Host and rabies virus gene expression is shaped by human brain cell type and reveals a preexisting pro-viral transcriptional state in astrocytes

Authors

Lena Feige[1,2#,] Karl Young[3], Juan Pablo Cerapio[4-8], Tatsuya Kozaki[9], Lauriane Kergoat[1], Valentina Libri[10], Florent Ginhoux[9,11-12], Milena Hasan[10], Lamya Ben Ameur[3], Gregory Chin[3], Zach Goode[3], Hervé Bourhy[1*] and Arpiar Saunders[3#$*]

[1] Institut Pasteur, Université Paris Cité, Lyssavirus Epidemiology and Neuropathology, F-75015, Paris, France

[2] Université de Paris Cité, F-75015, Paris, France

[3] Vollum Institute, Oregon Health & Science University, Portland, OR, 97239, USA

[4] Centre de Recherches en Cancérologie de Toulouse, INSERM UMR1037, Toulouse, France

[5] Toulouse University, Toulouse, France

[6] CNRS UMR 5071, Toulouse, France

[7] Institut Universitaire du Cancer-Oncopole de Toulouse, Toulouse, France

[8] Laboratoire d'Excellence 'TOUCAN-2', Toulouse, France

[9] Singapore Immunology Network, Agency for Science, Technology and Research, Singapore 138648, Singapore

[10] Single Cell Biomarkers UTechS, Institute Pasteur, 28 rue du docteur Roux, 75015 Paris, France, Université Paris Cité, Paris, France

[11] Shanghai Institute of Immunology, Shanghai JiaoTong University School of Medicine, 280 South Chongqing Road, Shanghai 200025, China

[12] Translational Immunology Institute, SingHealth Duke-NUS Academic Medical Center, 20 College Road, Discovery Tower Level 8, Singapore 169856, Singapore

# equal contribution
$ lead contact
*Correspondence: saundear@ohsu.edu (A.S.), herve.bourhy@pasteur.fr (H.B.)

Keywords: neurovirology, rabies virus, single-cell RNA-seq, host – pathogen interactions, astrocytes, microglial

Summary

Rabies virus (RABV) proteins play dual roles during the infection of complex neural tissue, the generation and spread of new virions and the active inhibition of cellular innate immune pathways, both contributing to rabies' lethality. While spatially-distinct RABV protein residues specializing in virus-centric and immune-inhibitory functions have been identified, how these dual functions interact to shape infection outcomes across diverse types of host brain cells is unknown. To "unmask" and study how innate immune inhibition affects the transcriptional regulation of the human and viral genome with cellular resolution, we performed single-cell RNA sequencing of co-cultured human brain cell types, comparing infection dynamics of a wild-type RABV isolate virus to a mutant virus in which six critical point mutations in the phosphoprotein (P) and matrix (M) RABV proteins selectively neuter antagonism of interferon- and NF-κB- dependent cellular responses. Our analysis reveals that RABV gene expression is shaped by host cell type and that wild-type RABV infection induces small-scale, cell-type conserved transcriptional programs that may support infection by hijacking transcriptional feedback systems that control pro-viral host cell factors while minimizing anti-viral responses. In contrast to accepted models, disinhibited innate immune signaling increases RABV transcriptional output across infected cell types. Most strikingly, we discovered a subpopulation of astrocytes that supports an average of 6-fold higher viral mRNA expression through a massive host cell transcriptional change involving ~38% of astrocyte expressed genes. Our analysis suggests that these astrocytes we term "pro-viral" are a rare subtype present in the human brain and are primed to play a protective role during viral infection in concert with interferon-sensitive microglia recalcitrant to infection.

Introduction

Viruses possess diverse mechanisms that shape the cellular and molecular properties of host cells through direct viral-host protein interactions. Due to historic technical limitations, the molecular consequences of these interactions have been difficult to characterize, especially across diverse primary cell types that constitute complex tissue such as the human central nervous system (CNS). The neurotropic Rabies virus (RABV) – a prototypic member of the negative-stranded RNA *Lyssavirus* genus – has evolved specialized mechanisms of immune evasion in the CNS, contributing to fatal encephalomyelitis and approximately 60,000 deaths annually[1]. Immune evasion is a critical feature of RABV pathogenesis, as the virus must travel undetected for long distances from peripheral muscle into the CNS, leveraging neurons and neuronal synapses for retrograde (dendrite-to-axon) transport[2]. Remarkably, neuronal viability and function are preserved during infection of isolate, non-cell culture adapted RABV strains as brains often show minimal macroscopic and histopathological alterations[3,4]. While neurons possess mechanisms to detect and respond to infection, neuronal immune responses are comparatively restricted to those of neighboring glia[5,6], functionally-distinct brain cell types that form intimate physical interactions with neuronal processes and perform myriad functions. Recent *in vivo* evidence suggests RABV can infect astrocytes and Schwann cells, challenging the notion of exclusive neuron-specific tropism[7–9]. Astrocytes in particular are crucial for IFN-β signaling during RABV infection[10] and can enter "reactive" molecular states in response to diverse insults, including viral infection[11]. Microglia too are involved in RABV pathogenesis[12], but it remains unclear whether viral antigens observed within microglia are due to active infection or because of phagocytosis of infected neuronal material. Despite this unresolved debate, numerous reports indicate microglia transcribe pro-inflammatory genes (such as *ISG15*, *OASL1*, *IFIT2*, *CCL5*, *CXCL10* and *IL-6*) in response to RABV infection[9,13–15]. To counteract cellular innate immune pathways, RABV proteins evolved mechanisms to sabotage the *nuclear factor 'kappa-light-chain-enhancer' of activated B-cells* (NF-κB)[16,17] and the Janus kinases (JAK) - Signal Transducers and Activators of Transcription (STAT) pathways[18–20], and thus potently inhibit host cell transcriptional responses downstream of interferon (IFN) type I signaling[21]. Although significant mechanistic insights have been made into immune inhibitory function of RABV proteins using cell lines, the consequences of these physical interactions on properties of infection in neurons and glia are largely unknown. Importantly, many viruses, including RABV, appear to have co-opted host cell proteins (including innate immune detectors[22]) for their life cycle[23], suggesting that infection outcomes may depend on a complex "arms race" between anti- and pro-viral factors[24], the nature of which remains to be fully elucidated.

In this study, we developed an experimental system using Tha isolate RABV, co-cultured stem cell-derived human brain cell types and single-cell RNA-sequencing (scRNA-seq) to discover how active inhibition of IFN and NF-κB signaling shapes transcriptional responses across the viral and human genomes at single-cell resolution. Of the five RABV proteins encoded by five genes in the negative-stranded RNA genome (**Figure 1A,B**), the phosphoprotein (P) and matrix protein (M) potently inhibit key pinch-points in cellular innate immune signaling. Specifically, P protein selectively binds and inhibits phosphorylated targets downstream of IFN signaling, including STAT1/2/3[18–20,25–27] transcription factors in the cytoplasm or nucleus, as well as TBK kinase[28]. M binds and inhibits RelAp43[16], disturbing NF-κB transcriptional complexes (**Figure 1C**). Foundational work has 1) shown that rabies adaptation to cell culture genetically erodes the potency of innate immune inhibition[21] and alters viral tropism *in vivo*[7] and 2) has identified mutations in outward facing residues in P (W265G, M287V; "2P")[29] and

143 M (R77K, D100A, A104S, M110L; "4M")[16] that prevent pSTAT1/2 and RelAp43 binding,
144 respectively, yet leave canonical viral functions intact[14] (**Figure 1D,E**). Thus, we sought to
145 "unmask" the otherwise potent innate immune inhibition of Tha virus using the 2P4M knock-in
146 mutations and study the consequences of intact and unmasked innate immunity on viral and
147 host transcriptional signatures across brain cell types.

148 Our analysis reveals several important discoveries. First, we show that Tha RABV gene
149 transcription is coupled to transcription of the host cell genome and shaped by the host cell
150 type. Second, we demonstrate that Tha virus induces a conserved transcriptional response in
151 both neurons and astrocytes, increasing RNAs encoding proteins that are likely "pro-viral" and
152 thus promoting infection, while decreasing RNAs encoding interferon-related transcription
153 factors that control anti-viral responses. Third, we show, counterintuitively, that 2P4M-based
154 disinhibition of innate immune signaling *increases* viral transcription across cell types.
155 Increased viral transcription is most strikingly observed in a subpopulation of "pro-viral"
156 astrocytes, likely enabled by large-scale changes in the astrocytic molecular milieu including
157 increased expression of NF-κB effectors and reduced expression of genes supporting protein
158 translation and mitochondrial function. Additional analysis suggests that "pro-viral" astrocytes
159 are likely a rare subpopulation present in nominally uninfected human brain. Finally, we
160 demonstrate that microglia are almost completely recalcitrant to infection but nonetheless
161 respond to infection of other cell types through an interferon-stimulated gene (ISG) expression
162 response that is potentiated by both higher viral titer and 2P4M mutations. Through the lens of
163 gene expression, our data collectively suggest that innate immune inhibition by isolate RABV
164 maintains infection stealth by restricting viral gene expression, avoiding "pro-viral" astrocytes
165 and limiting ISGs in microglia.

166

167 Results

168 *Discerning infection states and host cell types from single-cell RNA sequencing data*

169 To study how isolate Tha RABV alters the molecular properties of human brain cell types at
170 single-cell resolution - and to "unmask" and then characterize how antagonism of IFN and NF-
171 κB by Tha RABV P- and M-proteins sculpt these changes through regulation of both the human
172 and Tha RABV genome - we performed scRNA-seq analysis (10x Genomics Chromium 3'
173 v3.1) of co-cultured human neurons, astrocytes and microglia 48 hours after bath application
174 of Tha (multiplicity of infection (MOI) 0.5 or MOI 5) or Tha2P4M (MOI 0.5) or from uninfected
175 control wells ("No Infection")(**Figure 1F**). Brain cell co-cultures were seeded with
176 approximately equal proportions of hNSC-derived neurons and astrocytes (~47% each) as well
177 as a small population of human-induced microglia (~6%)(**Methods**). The presence of these
178 differentiated cell classes and Tha RABV infection was confirmed using a Tha virus expressing
179 eGFP followed by immunolabeling of cell-type-specific marker proteins (**Figure 1G**). After
180 quality control, our analysis focused on n=23, 457 single-cell RNA profiles derived from acutely
181 dissociated cells with >2,000 RNA transcripts (as defined by unique molecular identifiers;
182 UMIs) collected across multiple biological replicates (No Infection control, n=3; Tha(0.5), n=3;
183 Tha(5), n=2; and Tha2P4M (0.5), n=2)(**Methods**; **Figure S2A,B**).
184
185 We next sought to accurately distinguish infected cells and uninfected "bystander" cells and
186 assign host cell type identities to each RNA profile. Because infected cells may contain variable
187 levels of viral mRNA, and bystander cells may accrue viral transcripts by chance during cell
188 dissociation and scRNA-seq library preparation, we developed a data-driven computational
189 approach using expectation-maximization to iteratively refine viral RNA distributions for

190 infected and bystander populations, accounting for variability in viral RNAs driven by biological
191 and technical factors (**Figure 2A,B**; **Methods**). The resulting "viral load" distributions – defined
192 as the percentage of total cellular mRNA derived from the Tha genome – clearly delineated
193 populations of infected and bystander cells (Infected, mean = 3.9±0.03 sem; range: 0.38 –
194 64.8; Bystander, mean = 0.17± 0.002 sem; range: 0-0.64)(**Figure 2C**). Simulated viral
195 expression data based on these inferred distributions closely matched that of real data,
196 confirming the accuracy of our approach (**Figure S2C**). Throughout this study, we use both
197 qualitative infection categories as well as a quantitative metric of infection progression ("viral
198 load") to guide our analysis of host and virus gene expression relationships at single-cell
199 resolution.

200 To assign single-cell RNA profiles to transcriptionally-defined brain cell types, we clustered cell
201 profiles using only genes from the human genome (**Methods**). The resulting clusters
202 corresponded to 5 major brain cell populations: neural stem cells (10.7%; n=2,526), mitotic
203 cells 3.3%; n=781), astrocytes (16.9%; n=3,975), microglia (5.2%; n=1,218) and two groups of
204 neurons (*OTP*+ and *SHOX*2+, (31.2%; n=7,312 and 32.6%; n=7,645, respectively) (**Figure**
205 **1D**). Each clustered cell population was robustly delineated by hundreds of differentially
206 expressed genes, including well-established "markers" that confirmed cell type identities
207 (**Figure S2D**). Throughout our analysis, we used both OTP+ and SHOX2+ populations when
208 analyzing neurons. RNA expression relationships were consistent with a dynamic
209 developmental continuum visible in the two-dimensional UMAP embedding, with a population
210 of hNSCs differentiating into both neurons and astrocytes, as well as a population of markedly
211 distinct microglia, consistent with unique developmental and experimental origin.

212 We next evaluated the type and proportion of infected cells across cell types and Tha RABV
213 infection conditions (**Figure 2E**). While microglia exhibited strikingly low infection percentages
214 across all conditions (~1%), all other cell types exhibited infection percentages between 79.7-
215 91.1% at MOI 0.5 and 96.8-98.4% at MOI 5. We observed no differences in cell-type rate of
216 infection between Tha(0.5) and Tha2P4M(0.5), suggesting that mutations in the RABV P- and
217 M-proteins had little effect on infection probability. Collectively, our scRNA-seq data and
218 analysis framework confirm the tenets of our human cell type co-culture system experimental
219 system and enable properties of Tha infection and the consequences of innate immune
220 inhibition to be analyzed at single-cell resolution in the context of host cell type.

221

222 ***Tha2P4M mutations increase viral transcription***

223 We next sought to understand how RABV transcription is shaped by human host cell type and
224 the 2P4M mutations. Because *lyssavirus* infection involves both negative-stranded RNA
225 genomes and positive-stranded anti-genomes and transcripts, we first evaluated the genomic
226 locations of our Tha RABV scRNA-seq reads to determine which RNA species were counted
227 in our dataset. Consistent with exclusive mRNA capture and 3' RNA sequencing, we observed
228 sense-read pileups immediately adjacent to viral polyadenylation signals, with negligible sense
229 or anti-sense reads mapped to other genomic locations. As expected, reads from bulk
230 sequencing of whole Tha mRNAs[30] fully covered the five RABV gene bodies (**Figure S3A,B**).
231 Next, we evaluated mRNA-based viral load distributions across cell types and experimental
232 conditions. We observed that mRNA viral load scores did vary by both cell type ($p < 4.8E-11$)
233 and experimental condition ($p < 2E-16$; ANOVA test). Strikingly, Tha2P4M(0.5) infections
234 exhibited a robust, consistent doubling of viral load across cell types (range of means = 4.8 –
235 7.7%) as compared to Tha(0.5) and Tha(5) infections consistently (range of means: Tha(0.5),

236 3.3 – 3.8%; Tha(5), 3.2 – 3.8%. These results indicate that disinhibited IFN and NF-κB
237 signaling is unexpectedly associated with an increase rather than a restriction of viral
238 transcription across cell types. Moreover, a subset of Tha2P4M infected astrocytes exhibited
239 strikingly high viral load scores (>10%) not observed in other Tha2P4M infected cell types
240 (**Figure 3A,B** and **Figure S3C**). Since the 2P4M mutations do not directly alter the function of
241 RABV transcription or replication[14], these data suggest that activation of innate immune
242 signaling by 2P4M mutations may alter the molecular milieu of Tha RABV-infected cells in
243 ways that contribute to higher levels of viral transcription, an effect that is especially
244 pronounced in a subpopulation of human astrocytes. Therefore, these results confirm that one
245 key function of wild-type Tha P and M proteins is to indirectly restrict viral RNA expression by
246 modulating molecular responses downstream of IFN and NF-κB transcriptional regulators in
247 infected cells.

248

249 ***Tha RABV gene expression is shaped by host cell type and viral mutations that restore***
250 ***host innate immune responses***

251 We next asked whether the transcription of *individual* Tha RABV genes is shaped by host cell
252 type and 2P4M mutations, as we observed for aggregate viral mRNA expression. Foundational
253 work of *rhabdovirus* transcription in cell lines has established the accepted "start-stop"
254 transcriptional model, in which the output of the RABV transcriptional complex (composed of
255 RNA-dependent RNA polymerase L and the phosphoprotein P) tracks the viral genome order
256 (3′ *N-P-M-G-L* 5'), with *N* RNAs expressed at the highest levels and *L* RNAs expressed at the
257 lowest levels[31–33]. After the RABV transcription complex binds to the nucleoprotein wrapped 3'
258 end of the negative-stranded RNA genome and transcribes the non-polyadenylated leader
259 RNA, each intergenic region probabilistically causes the transcriptional complex to dissociate,
260 leading to reduced gene-specific occupancy and a decline in expressed RNA (**Figure 3C**).
261 Interestingly, both bulk and scRNA-seq measurements of Tha mRNAs levels were not strictly
262 explained by genome order, with N, P, and M expressed at high levels and *G* and *L* at much
263 lower levels (range mean % viral mRNA, bulk: *N* = 24.3-24.6, *P* = 32-33, *M* = 38-38.2, *G* = 3.3-
264 3.7, *L* = 0.8-1.0, scRNA: *N* = 29-31, *P* = 44-46, *M* = 21-22, *G* = 0.9-1.2, *L* = 1.1-1.2)(**Figure**
265 **S3B**). While cross-gene expression comparisons are potentially influenced by the
266 methodologies used to prepare sequencing libraries, intra-gene expression comparison across
267 scRNA profiles are unaffected by these potential technical artifacts. Therefore, we compared
268 the relative expression of each Tha RABV gene to total viral RNAs across scRNA profiles
269 stratified by cell type and infection condition. Because the accepted "start-stop" transcriptional
270 model includes no role for feedback from host cell type or molecular state, we hypothesized
271 that 2P4M mutations and host cell type should not influence the expression of each Tha gene.
272 In contrast to our hypothesis, we observed influences of the both cell type and the Tha infection
273 condition on relative expression of Tha RABV genes (**Figure 3D** and **Figure S3C,D**). Most
274 strikingly, across all Tha RABV infection conditions, relative *L* RNA levels were doubled in
275 neurons compared to astrocytes (mean % *L* of viral RNA, Neurons: 1.9±0.01 sem; Astrocytes:
276 0.99±0.02; $p < 2E-16$; Mann-Whitney test). While MOI had only a marginal effect on Tha gene
277 expression by host cell type (**Figure S3D**), *N* and *P* levels differed across Tha2P4M infected
278 neurons and astrocytes ($p < 2E-16$; Mann-Whitney test), with neurons having slightly lower
279 levels of *N* (mean %, Neurons: 26.8±0.11 sem; Astrocytes: 28.6±0.24) and slightly higher
280 levels of *P* (mean %, Neurons: 47.3±0.08 sem; Astrocytes: 43.9±0.19) RNAs (**Figure 3D**).
281 These results suggest that the amount of different Tha RABV mRNAs is sculpted by host cell

type and that disinhibited innate immune signaling subtly alters viral gene transcription and/or the stability of the corresponding viral mRNAs in a cell-type-specific manner.

Tha RABV infection induces a cell-type-conserved pro- and anti-viral transcriptional response involving a small number of genes

Viral infections - including by various strains of RABV – can alter transcriptional regulation of the host cell genome in ways that have complex effects on host cell and tissue function[30,34,35]. However, systematic molecular descriptions of how isolate RABV infection might alter the transcriptome of distinct human brain cell types – including the consequences of innate immune antagonism induced by wild-type P and M proteins – have yet to be described at single-cell resolution. Therefore, we compared genome-wide expression data across cells stratified by cell type and experimental condition to evaluate how Tha RABV infection and 2P4M-sensitive innate immune disinhibition shapes neuron and astrocyte specific transcriptional responses.

To characterize transcriptional changes driven by Tha RABV infection and compare these changes across distinct host brain cell types, we performed genome-wide differential expression testing across cell-type-identified scRNA profiles from Tha RABV-infected (Tha0.5) versus “No Infection” cells, with a primary focus on neurons and astrocytes (**Figure 4** and **Figure S4A**; **Table S1; Methods**). Using false-discovery rate corrected p-values (FDR < 0.05) as a threshold, we identified 13 and 60 differentially expressed genes (DEGs) in neurons and astrocytes, respectively (**Figure 3A**). To determine the degree to which transcriptional responses to Tha RABV infection were shared or unique across neurons and astrocytes, we compared gene-specific fold-change for all differentially expressed genes in astrocytes or neurons while also tracking gene expression level in uninfected neurons (**Figure 3B**). Neuron and astrocyte specific responses to Tha-infection were well-correlated (r = 0.64), with a small set of human genes robustly induced in each cell type; genes with significant reductions in astrocytes also tended to be reduced in neurons, but low baseline neuronal expression likely limited further reductions and the sensitivity of our testing. Shared, strongly induced RNAs include those from *DYNLL1*, *DYNLL2* and *HSPA8* genes and the long non-coding RNA *NRAV* (located in anti-sense orientation int the *DYNLL1* gene locus). The striking induction of *DYNLL1* and *DYNLL2* was also observed after infection of another negative-stranded RNA virus, Ebola[36], and could be driven by a positive transcriptional feedback pathway through which lower cellular availability of DYNLL1/2 (perhaps by viral sequestration of dynein-light chain proteins[37], including RABV P[38–40] and L[41]) disinhibits transcription of the *DYNLL1* gene locus through the ASCIZ transcription factor[42]. In turn, higher levels of DYNLL1/2 promote RABV transcription and replication, a pro-viral effect that depends on P and L binding[39,43]. *HSPA8* encodes a member of the HSP70 family that is induced upon infection of RABV and other viruses and promotes viral replication and transcription, likely due in part to interactions in RABV Negri Bodies[44]. *NRAV* too has described pro-viral functions[45]. RNAs depleted from Tha RABV infected cells were largely restricted to genes encoding components of the IFN signaling, including *STAT1*, *IRF9*, *IFIT1* and *ISG15*, supporting previous observations that wild-type Tha RABV infection is sufficient to suppresses IFN-induced expression of innate immune genes encoding detectors and early-stage infection effectors[14] (even to levels lower than those observed in uninfected cells)(**Figure S4B**). Gene expression comparisons based on ten-fold higher MOI (Tha5) resulted in highly similar transcriptional changes (**Figure S4A**). These results demonstrate that during Tha RABV infection - in which an average of ~3% of all mRNAs are viral (**Figure 3B**) - neurons and astrocytes tended to share changes in RNA levels

329 from just a handful of genes: increases in RNAs encoding host cell factors with described or
330 likely pro-viral functions, and reductions in RNAs associated with genes encoding IFN-
331 activated anti-viral transducer or effector proteins. In aggregate, these results suggest two
332 functionally distinct transcriptional signatures that likely promote RABV replication while
333 minimizing innate immune detection and response that are conserved across brain cell types.

334

335 ***Tha2P4M mutations unmask an astrocyte-specific transcriptional response to infection***
336 ***involving hundreds of genes***
337 To unmask and compare the transcriptional responses inhibited by wild-type Tha P and M
338 proteins across brain cell types, we performed differential expression testing of infected, cell-
339 type-identified scRNA profiles across Tha(0.5) and Tha2P4M(0.5) conditions (**Figure S4A**).
340 We observed 15 DEGs in neurons, 14 of which were upregulated (**Figure 4C**). This
341 upregulated gene set included a subset of those same IFN-related genes that were
342 downregulated in Tha RABV-infected astrocytes (*IRF9, ISG15, SAMD9, STAT1, PLSCR*),
343 demonstrating this downregulation by Tha RABV infection was driven by effects downstream
344 of wild-type P and M proteins. Astrocytes, however, exhibited significant expression changes
345 in 445 up or down-regulated genes (**Figure 4C**). Gene-specific fold change comparisons to
346 neurons confirmed that a small subset of the upregulated genes in Tha2P4M-infected
347 astrocytes were cell-type conserved (n=6 of 204), while the vast majority of upregulated genes
348 (n=198 of 204) and nearly all down-regulated genes (n=241) were unique and selective to
349 astrocytes (**Figure 4D**). These results demonstrate that host brain cell type plays a profound
350 role in the breadth and capacity for transcriptional responses triggered by innate immune
351 signaling pathways typically inhibited by wild-type Tha P and M proteins. Analysis of enriched
352 Biological Pathway gene sets in these 445 genes underscored that genes selectively induced
353 in Tha2P4M-infected astrocytes were associated with innate immune responses and viral
354 infection (**Figure 4E; Methods**).

355

356 ***A subpopulation of astrocytes endows a pro-viral RNA cellular environment through a***
357 ***massive transcriptional change***
358 We next determined whether the large-scale transcriptional response observed in the grouped
359 comparison of Tha2P4M infected astrocytes was driven by a specific subpopulation of
360 astrocytes. To do this, we clustered astrocyte scRNA profiles from all experimental conditions
361 using exclusively human genes. Our analysis identified a major (Cluster 1: n=3,759 cells;
362 94.6%) and a minor (Cluster 2: n=216 cells; 5.4%) astrocyte population (**Figure 5A**). The
363 experimental composition of Cluster 2 cells strongly deviated from the full dataset ($p<2.2E-16$;
364 Chi-square test), with a 3.5-fold enrichment of Tha2P4M infected astrocytes, yet all
365 experimental conditions, including "No Infection" co-cultures, contributed cells (**Figure 5B**).
366 Cluster 2 was also enriched for infected cells as compared to the full dataset (95% versus
367 68%; $p<2.2E-16$; Chi-square test)(**Figure 5B**). Based on our previous observation that a
368 subset of astrocytes had particularly high RABV expression (**Figure 3A**), we compared viral
369 RNA load scores for cells in Cluster 1 and Cluster 2 (**Figure 5A**). On average, viral load scores
370 were 6.3-fold higher in Cluster 2 than in Cluster 1 (mean viral load: Cluster 1, 2.2%±0.04 sem;
371 Cluster 2, 13.8%±0.7; $p < 2.2E-16$, Kolmogorov-Smirnov test)(**Figure 5C**). We conclude that
372 a subpopulation of transcriptionally unique astrocytes supports very high levels of Tha RABV
373 RNA expression. Thus, we refer to Cluster 2 astrocytes as "pro-viral". While pro-viral Cluster 2
374 astrocytes were observed without infection (~5%), astrocytes tended to adopt this pro-viral

375 molecular state following Tha RABV infection, especially when the 2P4M mutations were
376 present. These results demonstrate that wild-type Tha P and M proteins actively restrict the
377 emergence of this pro-viral state during astrocyte infection. A corollary conclusion is that the
378 pro-viral astrocyte molecular milieu promotes RABV transcription more so than in other cellular
379 contexts.

380 To quantify the magnitude of transcriptional changes distinguishing Cluster 1 and pro-viral
381 Cluster 2, we performed differential expression testing. Our analysis revealed significant
382 alteration in the RNA levels of 8,862 genes, equating to changes in ~38% of all astrocyte
383 expressed genes (Cluster 2 enriched: 2,343 genes; Cluster 2 depleted: 6,521 genes)(**Figure**
384 **5D**). To determine to what degree viral load contributed to these transcriptional differences,
385 we downsampled scRNA profiles such that viral load distributions were equivalent across
386 clusters and repeated differential expression testing (n=276 cells in each cluster; **Methods;**
387 **Figure S5A,B**). Gene-specific fold change values were highly correlated across the full and
388 downsampled analysis (r = 0.82), with 32% of significant genes shared in both comparisons.
389 The vast majority of other genes passing the significance threshold were observed in the full
390 dataset but had similar, non-significant directional changes in the downsampled data (**Figure**
391 **5E**), likely due to the drop in test sensitivity from far fewer cells in the analysis (n= 552 versus
392 3,975 scRNA profiles). These data suggest that the massive transcriptional changes in human
393 genes observed in pro-viral Cluster 2 are largely independent of high viral load.

394 We next tested whether the molecular state in pro-viral Cluster 2 affects the transcriptional
395 coupling between RABV and host cell genome during infection using *DYNNL1*. To do this, we
396 focused on the positive relationship between *DYNNL1* RNA levels and viral load, clearly
397 apparent when all Tha RABV-infected cells are stratified into low, medium and high viral RNA
398 load groups (**Methods**). Further stratification of scRNA profiles by cell type revealed that
399 *DYNNL1* RNA levels grew with viral load scores in neurons and Cluster 1 astrocytes but not in
400 pro-viral Cluster 2 astrocytes (Neurons, $p < 2E-16$; Cluster 1 astrocytes, $p < 2E-16$; pro-viral
401 Cluster 2 astrocytes, $p = 0.06$; Kruskal-wallis test)(**Figure 5F**). These results suggest that the
402 molecular properties of pro-viral Cluster 2 astrocytes fundamentally alter the transcriptional
403 coupling between RABV and host cell genome that occurs during infection of other cell types.

404

405 ***Identification of pro-viral Cluster 2-like astrocytes in the human brain***

406 The presence of ~5% of uninfected astrocytes in Cluster 2, including from uninfected co-
407 cultures, hinted that this pro-viral astrocytic transcriptional state might exist independent of
408 RABV infection and motivated us to explore the possibility that Cluster 2-like astrocytes might
409 be present in human brains independent of RABV infection. To evaluate this possibility, we
410 took advantage of a snRNA-seq dataset acquired from flash-frozen cortical tissue resected
411 during Normal Pressure Hydrocephalus (NPH) surgery[46], enabling analysis of *ex vivo* astrocyte
412 RNA profiles from 52 living patients. Therefore, these cortical samples were collected without
413 the confound of post-mortem interval nor acute central nervous system infection. To search for
414 Cluster 2-like astrocytes in the 82,634 NPH snRNA-profiles from astrocytes, we developed an
415 aggregate expression score approach, leveraging genes highly enriched (> 2 log2 fold-change)
416 in pro-viral Cluster 2 astrocytes to create a "discovery" gene set (**Figure 5G-I**; **Methods**). As
417 expected, aggregate expression of this Cluster 2 "discovery" gene set (n=268 genes) clearly
418 distinguished Cluster 1 and Cluster 2 scRNA profiles in a manner independent from our original
419 analysis, confirming the approach's sensitivity (**Figure 5G**). We then calculated aggregate
420 expression scores for NPH astrocyte snRNA-seq profiles based on the 196 "discovery" genes

421 expressed in both datasets. To contextualize the distribution of "discovery" gene set scores
422 and define a false-discovery threshold, we performed a similar analysis on n=1,000 permuted
423 gene sets of 196 genes matched for expression level. We then calculated gene set-specific z-
424 scores to directly compare the "discovery" and permutation results (**Figure 5H**; **Methods**). In
425 support of Cluster 2-like astrocytes present in living human cortex, we observed a small
426 number of snRNA profiles with very high "discovery" set z scores (up to 12.5 standard
427 deviations above the mean) not observed in the permutations. Using a z-score threshold of 4.5
428 (corresponding to a p value cut off of 4.7E-7 based on the permutations), we identified n=38
429 Cluster 2-like astrocytes contributed by 21 of 52 total patients (n=1 to 4 Cluster 2-like NPH
430 astrocytes per patient, ranging from 7 to 4,990 total astrocyte snRNA profiles per patients
431 (median: 1,278). We reasoned that if these 38 single-nucleus RNA profiles were indeed Cluster
432 2-like, they should also be enriched for an independent gene set with enriched expression in
433 pro-viral Cluster 2 astrocytes. Indeed, a "validation" gene set of 521 genes with RNAs 1-2 log2
434 fold-enriched in Cluster 2 astrocytes also had enriched expression in the 38 snRNA-profiles as
435 compared to all other NPH astrocytes (n= 82,596: $p < 2E-16$, chi-square test). The degree of
436 "discovery" and "validation" gene set enrichment in NPH astrocytes corresponded to the
437 predictions from pro-viral Cluster 2 astrocytes (NPH expression enrichment: "discovery", 2.8;
438 "validation", 1.2)(**Figure 5I**). Collectively, these analyses provide preliminary support for a rare
439 (~1 in 2,200) population of pro-viral Cluster 2-like astrocytes in human cortex without acute
440 infection of the central nervous system.
441
442

443 ***Transcriptional analysis identifies major cell-autonomous and nonautonomous***
444 ***functional changes of pro-viral astrocytes***
445 We next sought to analyze how the massive transcriptional changes distinguishing Cluster 1
446 from pro-viral Cluster 2 astrocytes might alter both intercellular interactions with other cell types
447 and cell-autonomous astrocyte function. Importantly, we found no evidence that the pro-viral
448 transcriptional state we observed in Tha2P4M infected human astrocytes was previously
449 documented in cultured or *ex vivo* rodent and human astrocytes experimentally driven into
450 "reactive" states through interferon[47,48] or lipopolysaccharide exposure (**Figure S6A**).
451
452 To understand to what degree the pro-viral transcriptional state affects astrocyte signaling with
453 other co-cultured brain cell types, we leveraged CellPhoneDB(v5.0), a database of pairwise-
454 protein interactions that includes both secreted and extracellular ligands in relationship to
455 receptor complexes. We focused our analysis on genes with > 1 log2 fold-enrichment in either
456 Cluster 1 (n=2,186) or Cluster 2 (n=877). CellPhoneDB uses cell-type-assigned scRNA-seq
457 data and a gene-shuffling permutations to identify "relevant" ligand-receptor interactions that
458 are selectively enriched in target gene sets over background expression in other cell types (p
459 < 0.05 based on permutations). CellPhoneDB analysis revealed that pro-viral Cluster 2
460 astrocytes tended to express fewer "relevant" ligand and receptor genes than Cluster 1
461 astrocytes, suggesting a global reduction in the capacity for intercellular signaling (**Figure 6A**).
462 Interestingly, the more minor subset of ligands upregulated in pro-viral astrocytes include
463 immune effectors that function as secreted chemokines (*IL34*, *LIF*, *EDN1*) or extracellular
464 glycoproteins (*VCAM1* and I*CAM1*). In some cases, ligands or receptors from the same
465 signaling family exhibited bi-directional changes in RNA levels. For example, *WNT3A* and
466 *VEGFA* (ligands) and *EPHA4* (receptor) were enriched while *WNT7B* and *VEGFB* (ligands)
467 and *EPHB1* (receptor) were reduced in pro-viral Cluster 2 Astrocytes. Analysis of "relevant"

468 ligands and receptors in the context of RNAs expressed by other co-cultured brain cell types
469 suggested that pro-viral Cluster 2 astrocytes (as compared to Cluster 1 astrocytes) exhibit
470 reduced signaling capacity to all major cell types to approximately the same degree. These
471 data also imply that pro-viral Cluster 2 astrocytes are cut-off from receiving interactions from
472 other cell types (save from other pro-viral and Cluster 1 astrocytes)(**Figure 6B**). These RNA-
473 based inferences suggest that pro-viral Cluster 2 astrocytes are poised to send and receive
474 fewer total cellular interactions yet highlight a small number of key signaling pathways through
475 which astrocytes in the pro-viral molecular state might "advertise" to other brain cell types.
476
477 We next leveraged gene expression changes to build testable hypotheses for how the pro-viral
478 transcriptional state might affect cell-autonomous function of human astrocytes. To find
479 themed structure in the ~38% of astrocyte-expressed genes differentially expressed across
480 Cluster 2 and Cluster 1 astrocytes, we performed hierarchical clustering of REACTOME
481 categories based on shared genes up regulated in Cluster 1 (n=6,521 genes; n=84 categories,
482 p <1E-6) or Cluster 2 (Cluster 2, 2,343 genes; n=32 categories, p<1E-3)(**Figure 6C**). These
483 results implicate a diverse set of cellular processes affected by the large-scale restructuring of
484 the pro-viral astrocyte transcriptome. Due to the number and complexity of these changes, we
485 focused further analysis on the following salient gene sets to more fully understand how
486 astrocytes in particular respond to infection: 1) genes controlled by "Toll-like receptor
487 cascades" (**Figure 6D**) and genes encoding machinery for 2) protein translation and 3)
488 mitochondrial respiration (**Figure 6E**). ("Toll-like receptor (TLR) cascades" is likely a proxy for
489 gene sets activated by the IRF3/IRF7/NF-κB transcription factor complex, which in the case of
490 RABV infection, is primarily driven through activation of viral sensors such as TLRs and RIG-
491 I-like receptors (RLRs)[49,50]).
492
493 To determine how the molecular milieu of Cluster 2 astrocytes is sculpted by RNA level
494 changes of genes controlled by "Toll-like receptor cascades", we ranked fold-changes for 108
495 associated genes (**Figure 6D**). This analysis highlighted the striking role for transcriptional
496 induction of both NF-κB and immediate early gene (IEG) transcription factors and regulators
497 (NF-κB: *NFKB1*, *NFKB2*, *NFKBIA*, *NFKBIB*; IEG: *JUN*, *FOS*) as well as induction of gene
498 targets controlled by both NF-κB and IEG transcriptional complexes (NF-κB: *BIRC3*, *BIRC2*,
499 *NOD2*, *RIPK2*, *IRAK1, TRAF2;* IEG: *DUSP4, DUSP6, DUSP3*). RNAs from this group depleted
500 in the pro-viral state encode MAP kinases and regulators (*MAP2K6*, *MAPK10*, *MAPK3*,
501 *MAPK14*, *MAPKAPK3*, *MAPK8*, *MAPK7*) as well as ubiquitin and ubiquitin regulators (*UBB*,
502 *UBA52*, *UBE2V1*, *UBC*, *UBE2D1*, *UBE2N*, *UBE2D2*). Thus IRF3/IRF7/NF-κB activation
503 downstream of viral sensor activation contributes to the pro-viral state through potent activation
504 of NF-κB genes and targets and depletions of RNAs that likely alter MAPK kinase and ubiquitin-
505 based protein degradation. Intriguingly, *BIRC3* and *RIPK2*, the two genes with the largest fold-
506 change, encode anti-apoptotic (BIRC3) and pro-necrotic (RIPK3) proteins, potentially
507 contributing to the fate of pro-viral astrocytes.
508
509 To determine how transcriptional alterations of genes encoding protein translation and
510 mitochondrial function might contribute to the function of pro-viral astrocytes, we assessed
511 expression-level changes of ribosomal subunits, tRNA synthetases and the COX and NDUF
512 gene families encoding Complex IV and Complex I of the electron transport chain, respectively
513 (**Figure 6E**). Pro-viral astrocytes exhibit potent reductions in RNAs encoding nearly all subunits
514 of the cytosolic ribosome (n=85 genes), and bi-directional regulation of mitochondrial ribosome
515 subunits (n=78) and tRNA synthetases (n=37 genes). Most members of the COX and NDUF

516 gene families had reduced expression in pro-viral astrocytes. These transcriptional changes
517 were highly-selective for pro-viral astrocytes, as RNA levels associated with these genes were
518 not different across No Infection and Tha(0.5) RABV infected astrocytes (**Figure 6E**). These
519 results suggest that pro-viral astrocytes likely have severely reduced or dysregulated capacity
520 for protein translation and oxidative phosphorylation, indicating a potential mechanism of "host
521 shut off" based on RNA level changes. Since RABV morphogenesis and infection viral particle
522 production relies on host cell translation and ATP production to produce infective virion, our
523 cell signaling and gene-set focused analyses suggest pro-viral astrocytes may create an
524 immune-stimulatory environment by fostering high levels of viral RNA while restricting
525 collateral infections. Tha RABV infection with wild-type P and M protein would efficiently inhibit
526 this theoretical outcome.
527
528 ***Microglia indirectly respond to infection of other cell types through interferon-***
529 ***stimulated genes potentiated by 2P4M mutations***
530 Lastly, we explored how RABV infection-resistant microglia indirectly respond to infection
531 properties of other susceptible co-cultured brain cell types and how these transcriptional
532 responses associate with Tha RABV titer or innate immune signaling disinhibited by 2P4M
533 mutations. To do this, we re-clustered microglia scRNA-seq profiles and tracked the
534 experimental origins of each library (**Figure 7A**). Three distinct analysis or visualization
535 approaches – including UMAP embeddings (**Figure 7A**), principal components analysis of
536 shared expression variance (**Figure 7B**) and differential expression analysis (**Figure S7C**) –
537 revealed that exposure to Tha RABV particles and the milieu of neighbouring infected cells
538 affect a graded transcriptional response of interferon-induced genes in microglia (e.g. *SNX10*,
539 *GBP1*, *IFIT2*, *ACSL1*) (**Figure 7C**). The number and degree of interferon-induced
540 transcriptional differences were largest in the Tha(5) condition, followed by Tha2P4M(0.5) and
541 then Tha(0.5)(**Figure 7D,E** and **Figure S7C**), as clearly evidenced by example gene RNA
542 levels (*ISG15, IDO1, and IFIT3*)(**Figure 7E**). Consistent with rapid induction and degradation[51],
543 RNAs encoding interferon proteins were not detected 48 hours after viral infection, obfuscating
544 the cellular source of interferons in our analysis. Importantly, in titer-matched experiments, the
545 interferon-related transcriptional response in microglia was larger with 2P4M-mutations
546 (**Figure 7C**), suggesting that disinhibited innate immune signaling and/or higher levels of viral
547 RNA in cells potentiate an interferon-stimulated gene responses in microglia.

548

549 ## Discussion
550 In this work, we characterized how the innate immune signaling inhibition conferred by RABV
551 P and M proteins shapes the transcriptional properties of the host and viral genomes across
552 human neurons and glia. While molecular mechanistic analyses in cell lines has described the
553 potent and synergistic ways that RABV M and P proteins inhibit the induction and response to
554 IFNs[18–20,25–28], the consequences of innate immune inhibition or disinhibition on host-virus
555 relationships were unknown. Here we used an experimental and analytical framework with
556 several key attributes to characterize these consequences in major human CNS cell types,
557 revealing important new insights into RABV-host cell interactions and how innate immune
558 antagonism shapes viral infection properties. These attributes include 1) the use of Tha RABV
559 derived from a field isolate (that exhibits profound innate immune inhibition as compared to
560 attenuated RABV strains more adapted to cell culture) and 2P4M mutations (that selectively
561 and potently strip away major RABV innate immune inhibitory mechanisms); 2) co-cultured
562 human stem-cell derived brain cell types, enabling human cell biology to be studied in a

563 relevant model of cross-cell type signaling; 3) single-cell RNA-seq phenotyping in which RNA
564 level across the RABV and cell-type identified human genomes are measured at cellular
565 resolution; and 4) novel analytical methods to qualitatively group infected and uninfected
566 scRNA-seq profiles across heterogenous infection states and the use of "viral RNA load" as a
567 quantitative proxy for infection state progression. (Viral RNA load varied considerably in
568 infected cells after 48 hours, from 0.4 to 65% viral mRNA, highlighting the importance of
569 tracking viral load when experimentally phenotyping individual cells).

570 Our results suggest two ways in which Tha RABV gene expression is not anticipated by the
571 accepted "start stop" transcriptional model. First, in both bulk mRNA and scRNA-seq based
572 datasets, Tha RABV RNA levels were not strictly explained by genome order, with *N*, *P* and *M*
573 levels high (~24-46% of viral mRNAs) and *G* and *L* levels much lower (~1-2%). While RNA
574 capture and library preparation methods can complicate cross-gene RNA level comparisons,
575 the lack of strict genome-ordered expression across independent methods suggests other
576 factors (such as post-transcriptional regulation) may need to be considered to fully understand
577 variable levels of RABV transcripts in infected cells. Second, scRNA-seq analysis suggests a
578 clear if subtle role for host cell type in shaping RABV gene expression. Most saliently, *L* RNAs
579 were observed on average at double the levels in neurons as compared to astrocytes,
580 differences that could be driven by either molecular or physiological differences in host cells.
581 Future experiments are warranted to fully validate and understand the functional
582 consequences of cell-type-specific RABV gene expression differences and to identify the
583 mechanisms driving these effects.

584 In Tha RABV-infected neurons and astrocytes, we discovered largely conserved bi-directional
585 transcriptional programs involving ~60 human genes that likely promote infection progression
586 by both boosting RNAs encoding known pro-viral proteins or reducing RNAs encoding anti-
587 viral transduces or effectors. For example, of the four genes robustly induced by Tha RABV
588 infection (*DYNLL1, DYNLL2, NRAV and HSPA8;* **Figure 4A***),* all have been shown to promote
589 viral replication in some contexts. Importantly, the products of the protein-coding genes
590 (DYNNL1, DYNNL2 and HSPA8) are bound and/or sequestered by RABV proteins during
591 infection. *DYNNL1/DYNNL2* encode light-chain dynein subunits targeted by RABV P[38,40,52] and
592 L[43] proteins. The long non-coding RNA *NRAV* spans exons 2 and 3 of *DYNLL1* gene locus in
593 the anti-sense orientation on chromosome 12 and promotes influenzae replication and
594 virulence[45] (the functional effects of *NRAV* on RABV pathogenesis are yet to be determined).
595 *HSPA8* encodes a member of the HSP70 family, a host cell protein recruited to RABV Negri
596 Bodies (the specialized viral organelles in which viral transcriptional and replication occur) and
597 promotes RABV replication[44]. Our data thus suggest that RABV (and perhaps other viruses[37])
598 evolved to sequester host cell factors transcriptionally regulated by hijackable negative
599 feedback systems, enabling pro-viral host factor production to match viral demand as infection
600 proceeds. Indeed, *DYNLL1* levels positively scaled with viral RNA load in neurons and Cluster
601 1 astrocytes (**Figure 5F**) and previous work identified a potential mechanism: DYNLL1
602 sequestration by P and L might disinhibit DYNLL1-based negative regulation of the ASCIZ
603 transcription factor which promotes *DYNNL1* transcription[42]. More experiments are required to
604 mechanistically understand these transcriptional feedback systems, including how *HSPA8*
605 RNA levels might be induced by HSP70 recruitment to Negri Bodies. The genes potently
606 downregulated by Tha infection include RNAs encoding proteins with central roles in anti-viral
607 responses. These include anti-viral effectors IFIT1 and ISG15, as well as core components of
608 the ISGF3 transcriptional complex (STAT1 and IRF9) responsible for inducing interferon
609 expression[53]. These results offer insight into the mechanisms through which Tha RABV

610 infection completely blocks interferon-stimulated gene expression, even after exogenous IFNα
611 stimulation[14]. While more work is necessary to determine exactly how anti-viral RNAs are
612 reduced during Tha RABV infection, wild-type P and M proteins are likely involved, as an
613 overlapping anti-viral gene set is strikingly induced in neurons infected by Tha2P4M (**Figure**
614 **4C**).

615 One major observation of our study is that 2P4M-based disinhibition of innate immunity results
616 in a mean doubling of viral load across cell types (**Figure 3A** and **Figure S3C**). Three pieces
617 of evidence suggest that increased viral transcription is an indirect effect of the disinhibited
618 innate immune milieu rather than a direct effect of the 2P4M mutations on the RNA-dependent
619 RNA polymerase L. First, the 2P4M mutations sit at residues independent and distant from
620 those known to bind or modulate L function[14,16,54]. Second, Tha and Tha2P4M have
621 indistinguishable replication properties in BSR-T7 cells that lack an IFN response[14]. Third, P/M-
622 based restriction of RABV transcription is cell type and state-specific, as observed in the "pro-
623 viral" astrocyte subpopulation that had on average six-fold higher viral load scores than other
624 neurons and astrocytes (Cluster 2; **Figure 5A,C**). Therefore, one important consequence
625 RABV innate immune inhibition is likely to restrict viral transcription.

626 Our discovery and characterization of "pro-viral" human astrocytes deepens the growing
627 appreciation of how astrocytes contribute immune functions in the human CNS[11,55,56]. Our *in*
628 *vitro* analysis suggests that the "pro-viral" molecular state – distinguished by RNA level
629 differences in ~38% of astrocyte expressed genes – exists independently of RABV infection
630 and viral RNA load. This is supported by 1) the presence of 5% uninfected "pro-viral" astrocytes
631 (including those from uninfected culture wells); 2) the presence of pro-viral like single-nucleus
632 RNA profiles sampled from cortical biopsies of presumably RABV free NPH surgical patients
633 (~1 out of 2,200; observed in 21 of 52 patient samples); and 3) the observation that "pro-viral"
634 gene expression signatures are largely retained after controlling for viral load differences.
635 However, the proportion of astrocytes in the "pro-viral" state tends to increase after Tha RABV
636 infection, is further increased by higher Tha RABV titer and is dramatically increased when the
637 2P4M mutations are present (**Figure S5C**). These data may suggest that the pro-viral state is
638 not induced by infection exclusively, but is present in normal human brain tissue and can be
639 activated through signaling by other infected cells, especially when 2P4M mutations disinhibit
640 innate immune responses.

641 We leveraged gene expression data to draw a preliminary description of how the large-scale
642 "pro-viral" state might affect astrocyte function and cellular interactions. Our analysis suggests
643 that the "pro-viral" state tends to reduce the number of molecular opportunities for cell signaling
644 to other brain cell types and the only unique interactions "pro-viral" astrocytes are poised to
645 receive are from other astrocytes (in contrast to other infected astrocytes, which maintain
646 receptors to interact with all other cell types in our co-cultures). Our analysis highlights a
647 number of key signaling molecules including both ligands (*HBEGF4*, *VEGF4*, *IL34*, *VCAM1*,
648 *ICAM1*, *WNT3A* and *EDN1*) and receptors (*EPHA4*, *SSTR2*) that merit further investigation for
649 "pro-viral" astrocyte function. Cell autonomously, "pro-viral" gene expression changes indicate
650 a dramatic increase in NF-κB target gene expression, predicted to alter MAPK function and
651 protein ubiquitination. We also observed cellular RNA level changes consistent with potent
652 reductions in ribosomal machinery for protein translation and mitochondrial machinery for
653 oxidative phosphorylation; changes that may reflect an astrocyte-specific form of "host shut
654 off". (To our knowledge, "host shut off" molecular programs have not been previously described
655 either in astrocytes or for RABV infection of any cell type). The uncoupled transcriptional
656 feedback between *DYNNL1* levels and viral load observed in "pro-viral" astrocytes (but not in

657 other cell types) may be an important feature of this process (**Figure 5F**). Astrocyte-based
658 abortive infections occur at higher frequency in lab-attenuated versus field isolate RABVs[57],
659 suggesting the intriguing possibility that the "pro-viral" state we observed at higher rates
660 following Tha2P4M infection might represent a transcriptional snapshot of the abortive
661 infection process[58]. High levels of viral RNA and with reduced protein translation might suggest
662 that "pro-viral" astrocytes create an immune-stimulatory environment through viral RNA while
663 minimizing the generation of infective virions. Astrocyte infection fate-mapping experiments
664 could help clarify if the pro-viral state leads to abortive infections or other outcomes[58].

665 Our study also sheds a new light on the role of microglia. Our analysis suggests that microglia
666 are almost exclusively recalcitrant to RABV infection (~1% infected, n = 10 of 859; **Figure 7**).
667 The susceptibility of human microglia to RABV infection has been a topic of scientific
668 debate[35,59,60] . Our findings indicate that human microglia do not play major roles in the
669 replication and spread of canine RABV. The presence of viral RNAs in the 1% of microglia we
670 classified as infected may also be attributed phagocytosed material from infected cells.
671 Further, the degree of microglial interferon-induced transcriptional differences was largest in
672 the Tha RABV(5) condition, followed by Tha2P4M(0.5) and then Tha RABV(0.5) (**Figure 7D,E**
673 and **Figure S7C**), suggesting that Tha RABV is not able to actively infect microglia and
674 antagonize intracellular innate immune pathways via P and M proteins, as observed in
675 susceptible CNS cells such as neurons and astrocytes. Thus our data suggest that microglia
676 play an important bystander role and are capable of responding to the effects of innate immune
677 inhibition from other RABV infected cell types and/or extracellular RABV particles by mounting
678 a graded anti-viral interferon-stimulated gene response (**Figure 7**). Future experiments should
679 identify the sources and ligands responsible for these responses in microglia.

680 Our study has important limitations and follow-up studies are necessary to more fully
681 understand the biological results we reveal. For example, our genome-wide molecular
682 phenotyping was restricted to polyadenylated RNA levels, yet direct measurements of RABV
683 negative-stranded RNA genomes, host and viral RNA isoforms, non-coding RNAs (including
684 RABV leader and trailer RNAs) along with chromatin remodeling data would be necessary to
685 measure at cellular resolution to more fully understand the molecular consequences of isolate
686 RABV infection and "unmasked" innate immune signaling. Additionally, more work is required
687 to fully understand the function of "pro-viral" astrocytes. Future experiments should 1) locate
688 and quantify "pro-viral" astrocytes through molecular anatomical analysis of human brain
689 tissue; 2) characterize the temporal progression and fate of the "pro-viral" state across different
690 conditions (infection both other viruses, aging and neurodegeneration, for example) and 3)
691 functionally assess how the "pro-viral" state affects astrocyte physiology and cell signaling.

692 Another limitation stems from the sex differences in the karyotypes of the cell types used in
693 this study. The iPSC-derived microglia used had a male karyotype, whereas the neurons and
694 astrocytes derived from human neural stem cells (hNSCs) had a female karyotype[61] . These
695 sex-specific differences may influence cellular responses and contribute to some of the
696 observed outcomes. Future studies would benefit from a systematic examination of how sex-
697 linked genetic and epigenetic differences and genetic variation affect RABV infection dynamics
698 in human brain cell models.

699 Despite these limitations, our single-cell RNA-seq analysis using the Tha/Tha2P4M RABV
700 study system in human brain cell-type co-cultures provides a powerful approach to discover
701 key features of host-RABV interactions and a road map for building testable hypotheses

regarding the dynamics and key molecular interactions that drive neurotropic infection in the brain.

Acknowledgements

We thank Anne Danckaert and Nathalie Aulner (UTechS Photonic BioImaging (PBI) core at Institute Pasteur Paris) for help with the image acquisition using the Opera Phenix Plus High Content Screening System (Perkin Elmer) and data analysis using the Columbus software (Perkin Elmer). PBI is a member of the national infrastructure France-BioImaging supported by the French National Research Agency (ANR-10-INBS-04). We acknowledge financial support of the Région Ile-de France (program DIM1Health, to H.B.), the Institut Pasteur (H.B.), the Sloan Foundation (to A.S.) and the NIH Brain Initiative (R01 MH130464, to A.S.). We thank all other members of the Saunders and Bourhy labs for helpful discussions of this work.

Author contributions

Conceptualization (LF, KY, HB, AS); Data Curation (ZG, JPC); Formal Analysis (KY, GC, LBA, AS); Funding acquisition (HB, AS); Investigation (LF, TK, LK); Methodology (LF, KY, AS); Project Administration (HB, AS); Resources (LF, VL, FG, MH); Software (ZG, AS); Supervision (HB, AS); Validation (LF, AS); Visualization (KY, GC, AS); Writing – original draft (LF, AS); Writing – review & editing (LF, KY, GC, HB, AS).

Declaration of interests

The authors declare no competing interests.

747
748
749

750 ## Figures

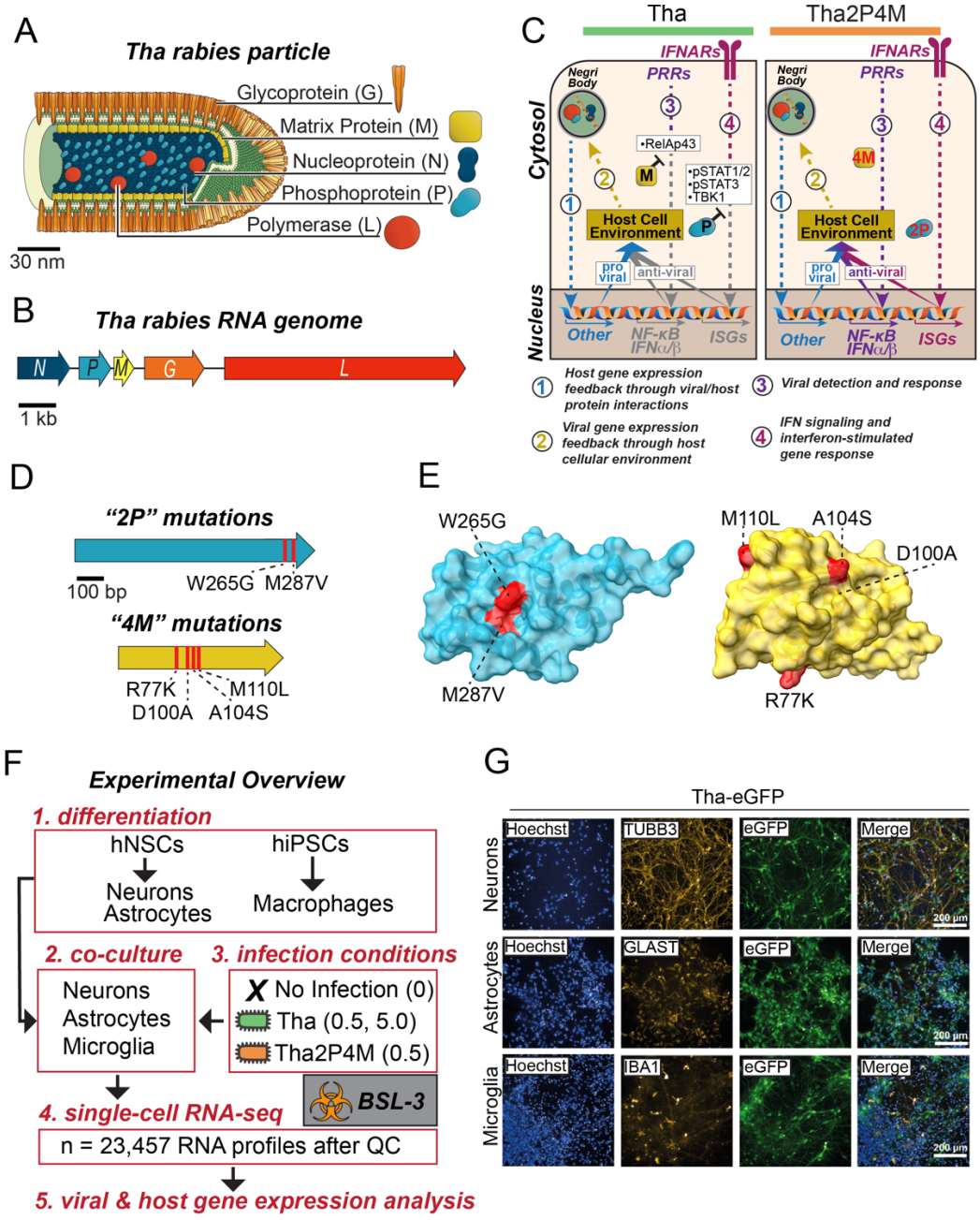

751

752 **Figure 1. Experimental overview for unmasking the molecular effects of innate immune**
753 **signaling inhibition across human brain cell types using field-isolate Tha RABV and**
754 **single-cell RNA-seq analysis.**
755 **(A-B)** Schematic illustrations of the RABV particle (A; modified from[2]) and genome (B) color-
756 coded by the five RABV genes and encoded proteins.

757 **(C)** Schematic illustrating known mechanisms of RABV P and M inhibition of viral detection
758 and response in Tha (*left*) or Tha2P4M (*right*) infection along with basic pathways (numbered

759 below) through which viral/host interactions and inhibited/disinhibited innate immune signaling
760 could affect viral and host cellular processes. Germline-encoded pattern recognition receptors
761 (PRRs) are viral sensors (such as toll-like receptors (TLRs); retinoic acid-inducible gene I (RIG-
762 I) like helicases (RLRs); and nucleotide-binding oligomerization domain-like receptors (NOD-
763 like receptors) that induce NF-kB and IFN pathways upon activation.

764 **(D)** Gene locations and amino acid alterations of six key point mutations that abolish innate
765 immune inhibition by P ("2P") and M ("4M") proteins.

766 **(E)** Protein structures of *lyssavirus* P (RABV CVS strain[62]) and M (Lagos bat virus[63]) highlight
767 the outward-facing locations of mutant residues in P and M (red). P mutations cluster around
768 the "W hole" (after[29]); M mutations affect three spatially-distinct interaction sites.

769 **(F)** Study system and scRNA-seq data generation overview. Human induced neural stem cells
770 (hiNSCs) or pluripotent stem cells (hiPSCs) were transformed into neurons/astrocytes or
771 macrophages and co-cultured, further inducing macrophage transformation into microglia.
772 Under Biohazard Safety Level 3 conditions, scRNA-seq analysis was performed on acutely
773 dissociated cells 48 hours after no viral infection (n=3 replicates) or bath application of Tha
774 virus at MOI 5 (Tha(5); n= 2 replicates) or MOI 0.5 Tha(0.5); n= 3 replicates) and Tha2P4M
775 virus at MOI 0.5 (Tha2P4M(0.5); n=2 replicates). After quality control, the final dataset
776 consisted of 23,457 RNA profiles and included 23,528 human and 5 RABV genes.
777 **(G)** Immunolabeling of cell type marker proteins on co-cultured cells after infection of Tha
778 RABV expressing eGFP, confirming the presence of infected human-induced neurons
779 (TUBB3), astrocytes (GLAST) and microglia (IBA1).
780
781
782
783
784
785
786
787
788
789
790
791
792
793
794
795
796
797
798
799
800
801
802
803
804
805

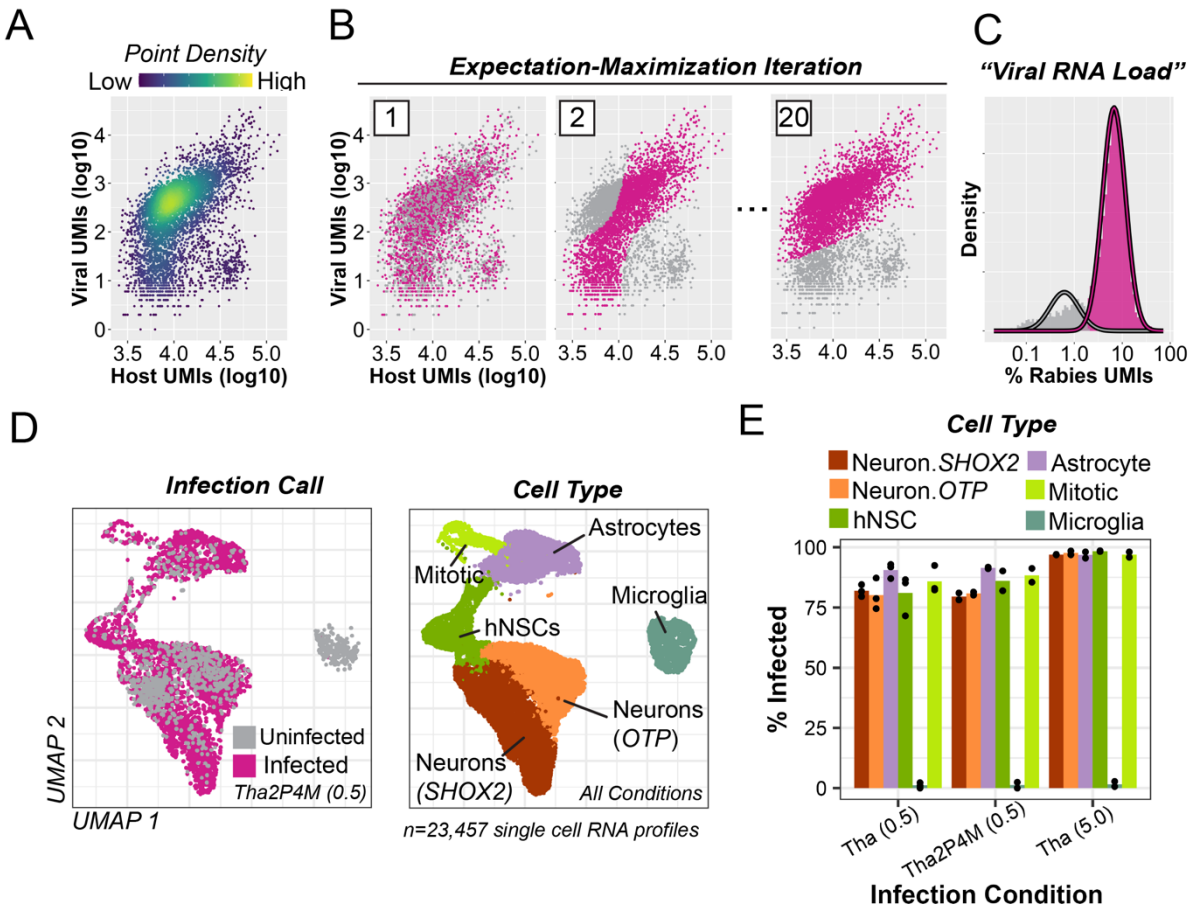

Figure 2. Transcriptional identification of infected and uninfected cell types

(A) Density plot comparing the number of viral UMIs versus total (viral + human) UMIs for each scRNA profile in the analysis.

(B) Systematic identification of infected and uninfected scRNA profiles using an Expectation-Maximization modeling approach to distinguish two cell populations based on viral UMIs (regressed by total UMIs)(**Methods**). Example results of infected (magenta) and uninfected (gray) scRNA profiles at iteration 1 (random assignment), iteration 2 and 20 (after convergence) are shown.

(C) Density plots of "viral RNA load" (the percentage of total UMIs that are viral) for scRNA profiles called as infected (magenta) or uninfected (gray).

(D) UMAP plot showing two dimensional embeddings of scRNA profiles following Seurat-based clustering analysis using exclusively human genes (**Methods**). scRNA profiles colored by infection status (*right*) or cell type-based cluster assignments (*left*).

(E) Barplots of the percent infected cells stratified by experimental condition and cell type.

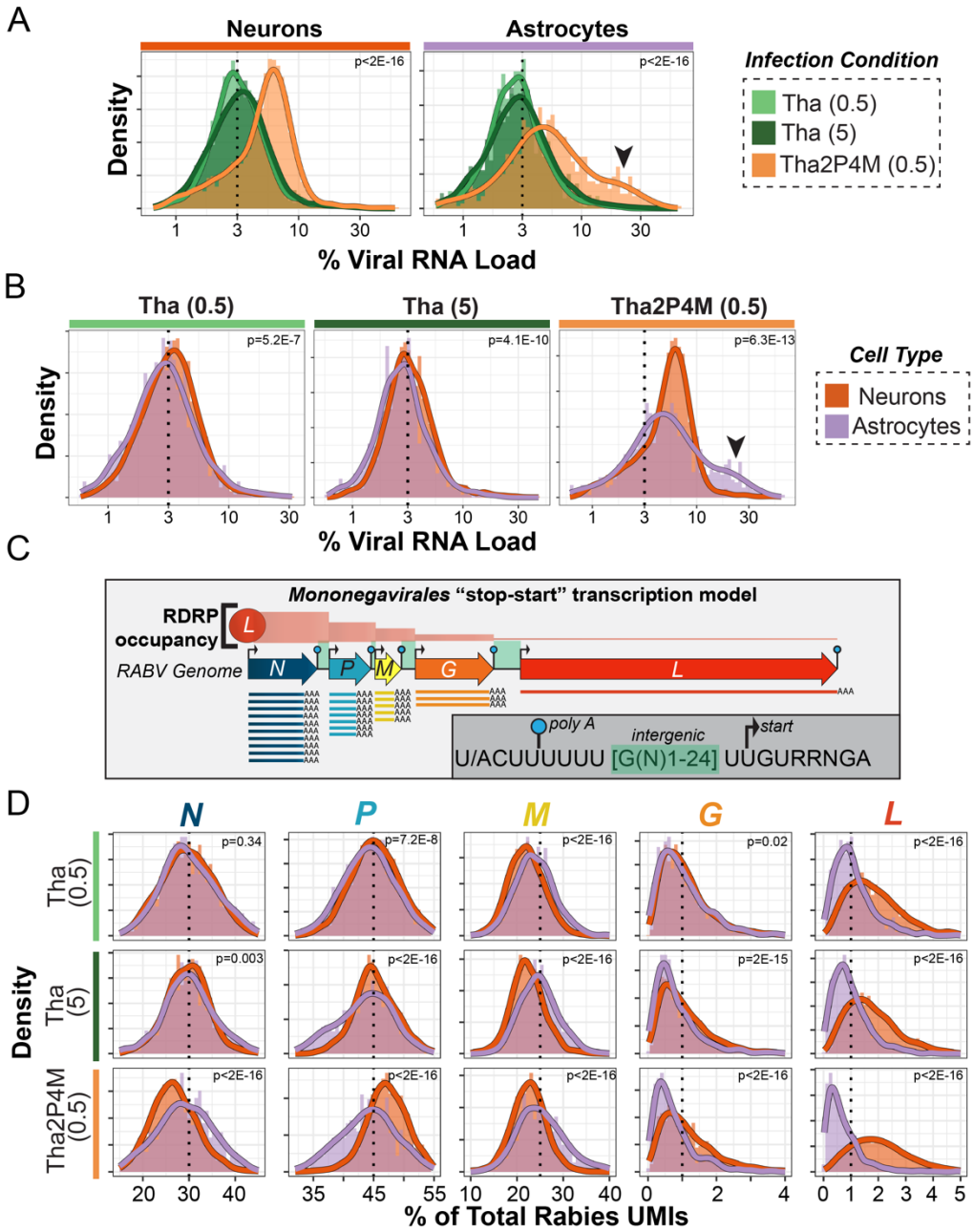

Figure 3. Tha2P4M mutations double viral RNA load without major alterations to cell-type-specific viral gene expression.

(A) Density plots of viral RNA load stratified by neurons and astrocytes and color-coded by experimental condition (n cells: Neurons, Tha(0.05) = 2,711; Tha(5) = 1,877; Tha2P4M(0.05) = 2,080; Astrocytes, Tha(0.05) = 1,036; Tha(5) = 798; Tha2P4M(0.05) = 806). Arrowhead indicates high viral RNA load astrocytes. Both cell type and experimental condition explain differences in viral load distributions (p<2E-16, Kruskal-wallis tests).

(B) Density plots of viral RNA load stratified by experimental condition and color-coded by cell type. Arrowhead indicates high RNA viral load cells in astrocytes. Same cells as in A. (Tha(0.5), p=1.1E-7; Tha(5), p=1E-14; Tha2P4M(0.5), p=0.58).

(C) Schematic of the accepted model of *lyssavirus* transcription, in which a genome-ordered RNA expression gradient is achieved by the RNA-dependent RNA polymerase (L). This model does not account for differences based on host cell type (after[2]).

(D) Density plots of relative RNA levels for each of the five Tha RABV genes color-coded by cell type and stratified by both gene identity and experimental condition. P values for differences in Neuron versus Astrocyte expression distributions are reported for each gene and experimental condition in the figure panel (Kolmogorov-Smirnov tests).

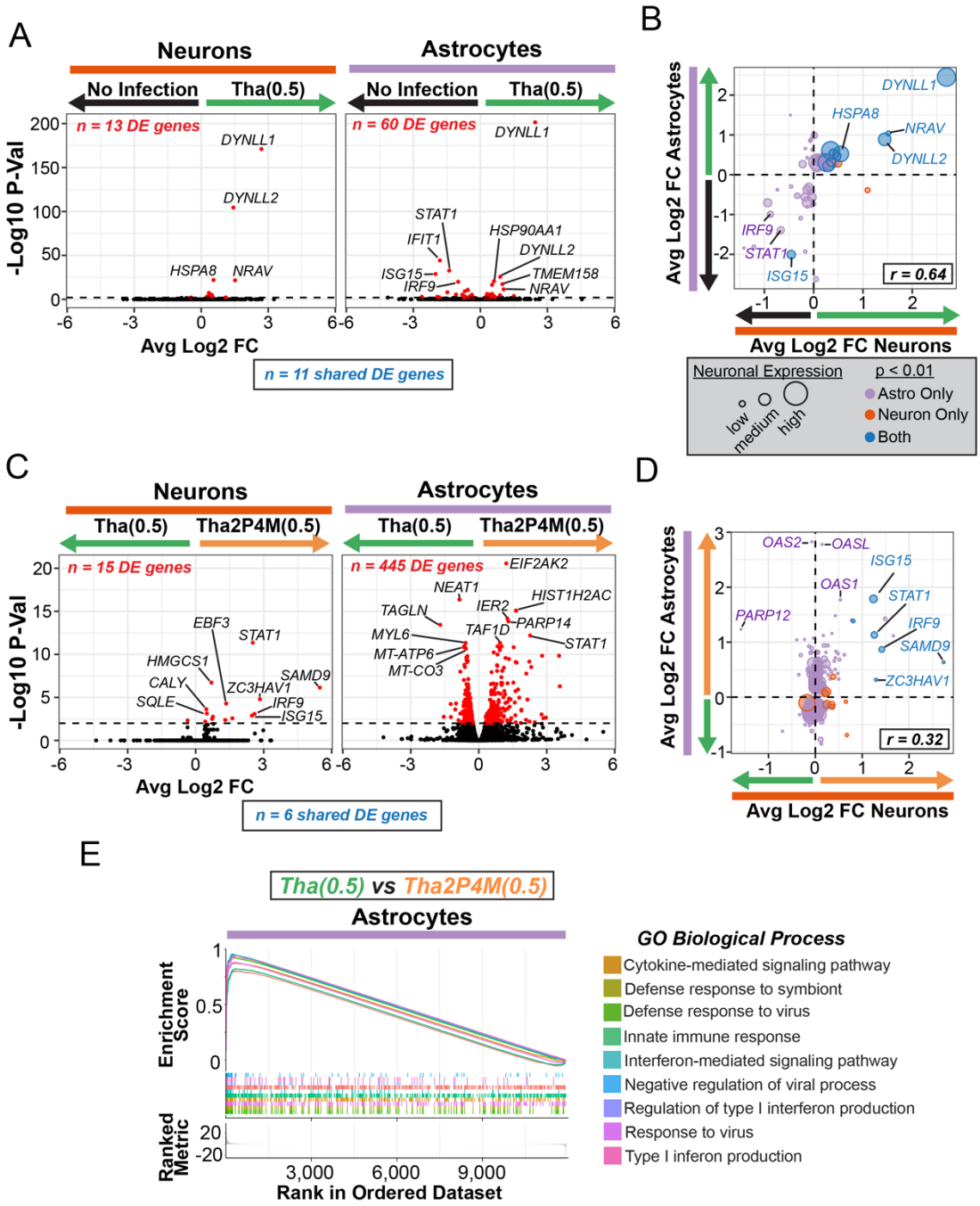

Figure 4. Tha2P4M mutations unmask a large-scale astrocyte-specific transcriptional response to infection.

(A-D) Genome-wide differential expression comparisons between neurons and astrocytes across no infection and Tha(0.5) infected (**A,B**) or infected Tha(0.5) and infected Tha2P4M(0.5) experimental conditions (**B,C**).

(A,C) Volcano plots of gene expression differences with select genes labelled (red, $p < 0.01$).

(B,D) Scatter plots comparing log2 fold expression level changes for genes significantly altered ($p < 0.01$) in either neurons (orange), astrocytes (purple) or both cell types (blue). Circle size is proportional to expression level in uninfected neurons.

(E) Gene set enrichment analysis of Biological Process Gene Ontology categories for differentially expressed genes ($p < 0.01$) across astrocytes infected with Tha(0.5) versus Tha2P4M(0.5) RABV. Gene set Enrichment Scores are shown for the nine most significantly enriched Biological Processes.

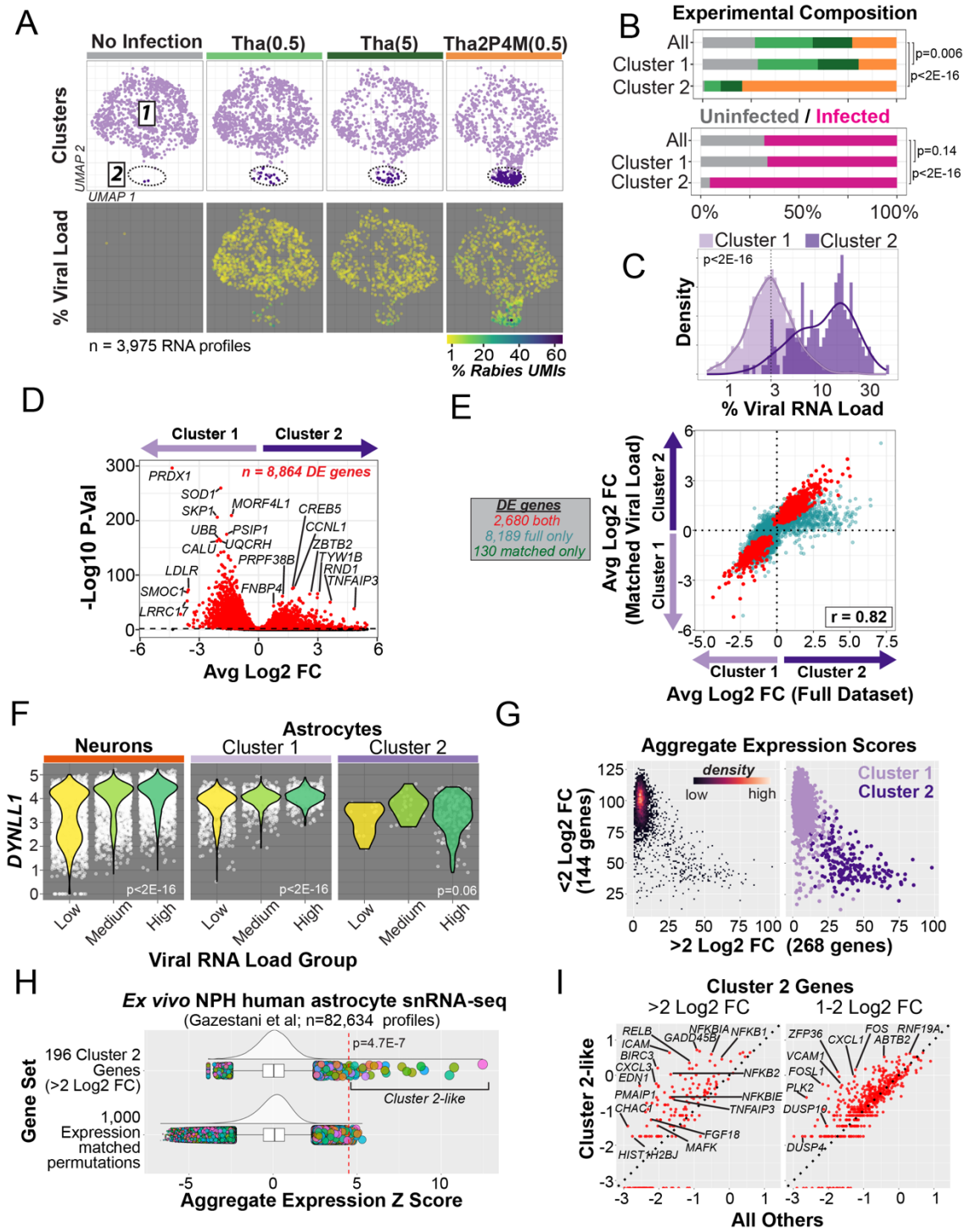

Figure 5. A pro-viral human astrocyte subpopulation supports high viral RNA load and is decoupled from typical host cell transcriptional feedback through a massive alteration in RNA levels.

(A) UMAP embedding plot of astrocyte scRNA profiles clustered exclusively by human gene expression differences and stratified by experimental condition (**Methods**). *Top*, color-coded cluster identities. (Cluster 1, n=3,759 cells; Cluster 2, n=216 cells). *Bottom*, heat map of viral RNA load scores.

(B) Bar plots comparing the composition single astrocyte RNA profiles from the full dataset versus Cluster 1 or Cluster based on experimental identity (Cluster 1 versus All: p=0.006; Chi-square test; Cluster 2 versus All: p<2.2E-16) or by infection status (Cluster 1 versus All: p=0.14; Cluster 2 versus All: p<2.2E-16).

(C) Combined histogram and density plot comparing viral RNA load distributions for Cluster 1 and 2 (p<2.2E-16, Kolmogorov-Smirnov test).

(D) Volcano plots of gene expression differences across Cluster 1 and 2 with select genes labelled (red, p < 0.01).

(E) Scatter plots comparing log2 fold expression level changes for genes significantly altered (p < 0.01) across Cluster 1 or Cluster 2 in the full dataset or a dataset in which viral RNA load scores were down-sampled to an equivalent distribution in Cluster 1 and 2 (**Methods**; **Figure S5A,B**). Differentially expressed genes are color-coded by membership (shared, red; full dataset only, cyan; equivalent viral load, green).

(F) Violin plots of *DYNNL1* expression levels stratified by both cell type and viral RNA load groups (Neurons, p<2E-16; Astrocytes Cluster 1, p<2E-16; Astrocytes Cluster 2, p=0.05. Anova test).

(G-I) Identification of rare "Cluster 2-like" astrocytes from single-nuclei RNA profiles derived from *ex vivo* cortical resections of living human Normal pressure hydrocephalus (NPH) surgical patients[46].

(G) Scatterplot of Cluster 1 or 2 astrocyte single-cell RNA profiles based on aggregate expression scores for genes up regulated in Cluster 1 (n=144 genes) or Cluster 2 (n=268 genes) (p < 0.01 and log2 fold-change > 2). *Left*, heat map of point densities. *Right*, color-coded cluster identities.

(H) Analysis of Cluster 2 aggregate gene scores for n=82,634 single-nucleus RNA profiles of astrocytes from n=52 NPH patients (median nuclei profile per patient = 1,277). Density and boxplots show aggregate expression z-score distribution for the 196 genes shared across both datasets (*top*) versus 1000 permutations of expression-matched NPH gene sets (**Methods**). snRNA-seq profiles > 4.5 standard deviations above the mean were considered "Cluster 2 like" (n=38 profiles identified in 21 of 52 total patients; p=4.7E-7 based on permutations). In box plots, outlier nuclei profiles > 1.5 interquartile range are shown as dots color-coded by patient identity with size proportional to aggregate gene z-score.

(I) Scatterplots of normalized metacell expression values for the 196 genes used to identify "Cluster 2-like" profiles (Identification Gene Set: p < 0.01 and >2 log fold-change; *left*) and for an independent set of n=521 gene RNAs with enriched expression in Cluster 2 astrocytes (Validation Gene Set: p < 0.01 and 1-2 log fold-change; *right*)(**Methods**). Metacells are composed of n=38 "Cluster 2-like" nuclei RNA profiles versus all other astrocyte nuclei profiles in the NPH dataset (n=82,596). Total UMI counts for both NPH gene sets were significantly enriched in "Cluster 2-like" NPH astrocyte profiles at levels that matched expectation from Cluster 2 (Identification Gene Set, 2.8 fold enriched; Validation Gene Set, 1.2 fold enriched; p<2.2E-16, Chi Square Test).

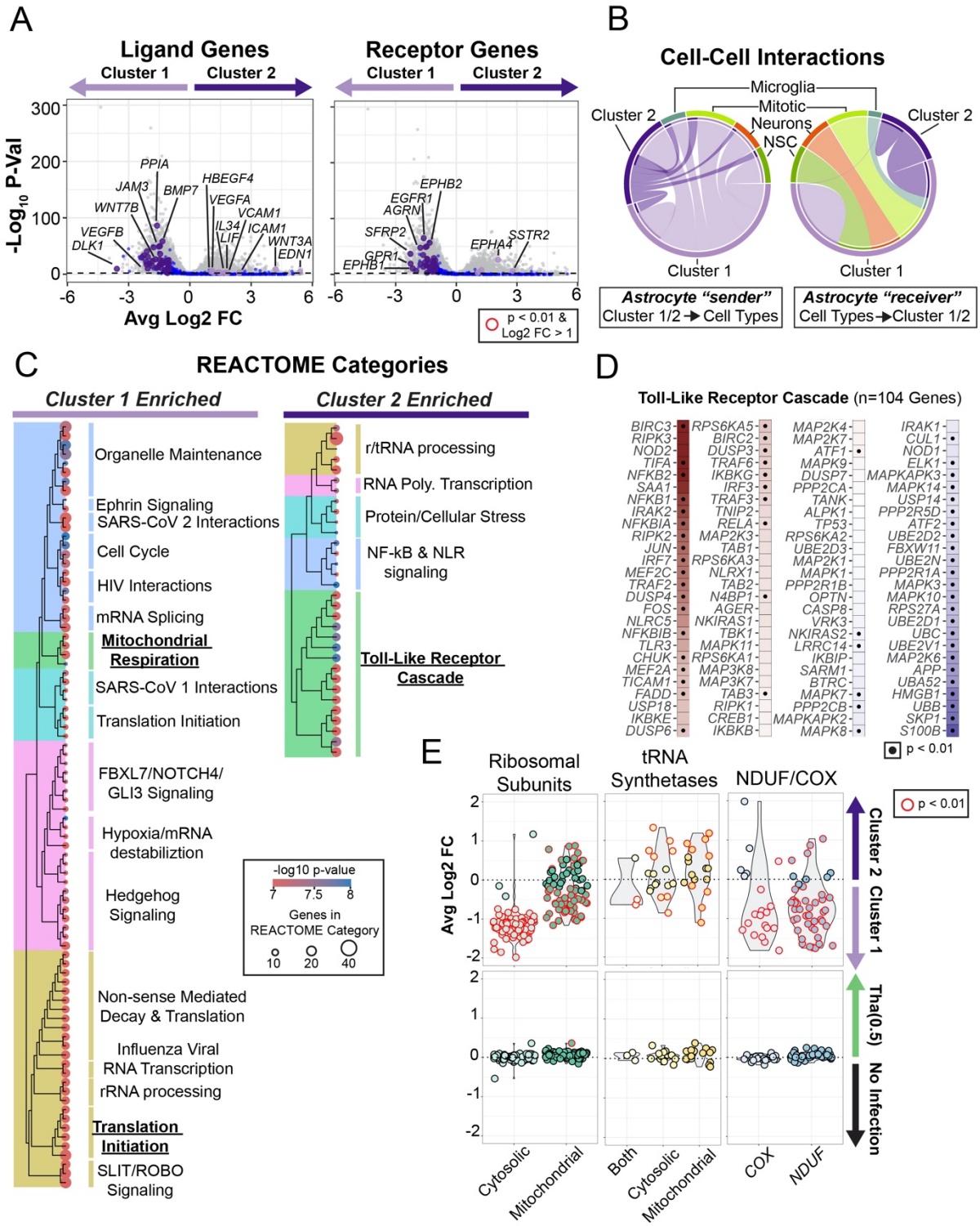

Figure 6. Gene expression changes in pro-viral human astrocytes imply reduced inter-cellular interactions, activation of toll-like receptors and complex changes in protein translation and mitochondrial respiration.

(A,B) Gene expression-based inference of alterations to inter-cell type interactions between Cluster 1 and Cluster 2 astrocytes using CellPhoneDB (CPDB) v5.0[64], a database of 1,419 molecular interactors (**Methods**).

(A) Volcano plot-based visualizations of ligand (*left*) or receptor (*right*) gene expression changes between Cluster 1 and Cluster 2. Ligand or receptor genes significantly enriched in either cluster ($p<0.01$) and significantly "relevant" (after CPDB permutation; $p < 0.05$) are circled in red (Ligand genes: Cluster 1, n=46; Cluster 2, n=11; Receptor genes: Cluster 1, n=32; Cluster 2, n=5). Other ligand or receptor genes are shown in blue and all other genes in gray.

(B) Chord diagrams showing the number of CPDB relevant interactions from (*left*) or to (*right*) Cluster 1 or Cluster 2 astrocytes for other cell types.

(C) Tree plot clustering of enriched REACTOME gene categories (Cluster 1: $p < 0.000001$, n=84 categories; Cluster 2: $p < 0.01$, n=32 categories) based on genes upregulated in Cluster 1 (*left;* n=6,551) or Cluster 2 (*right;* n=2,347)($p<0.01$). Hierarchical clustering results reflect shared genes driving each REACTOME category association. Dot size scales with the gene number in each category. Heat map indicates p value of each included category.

(D) Heat map plot reflecting log2 fold-changes in Cluster 2 of each gene in the Toll-Like Receptor Cascade REACTOME category (n=104 genes). Dots indicate significant expression changes ($p < 0.01$).

(E) Combined violin and dot plots reflecting gene-specific log2 fold-changes for gene sets encoding proteins related to translation (*left* and *middle*) or mitochondrial respiratory complexes I and IV (*right*). *Top row*, Cluster 1 versus Cluster 2 astrocytes. *Bottom row,* No Infection versus Tha(0.5) RABV infected astrocytes. Ribosomal subunit genes are stratified by whether the encoded protein is a component of cytosolic (n=85 genes) or mitochondrial (n=78 genes) ribosomes. tRNA synthetase genes are stratified by whether the encoded enzyme aminoacyl-tRNAs used for translation in the cytosol (n=17 genes), mitochondria (n=17 genes) or both ribosome types (n=3 genes). Nuclear gene components or assembly factors of the cytochrome c oxidase (COX) family (n=23 genes), Complex IV. The NADH:ubiquinone oxidoreductase (*NDUF*) family (n=47 genes) encoding Complex I. Red outlines indicate significant expression changes ($p <0.01$).

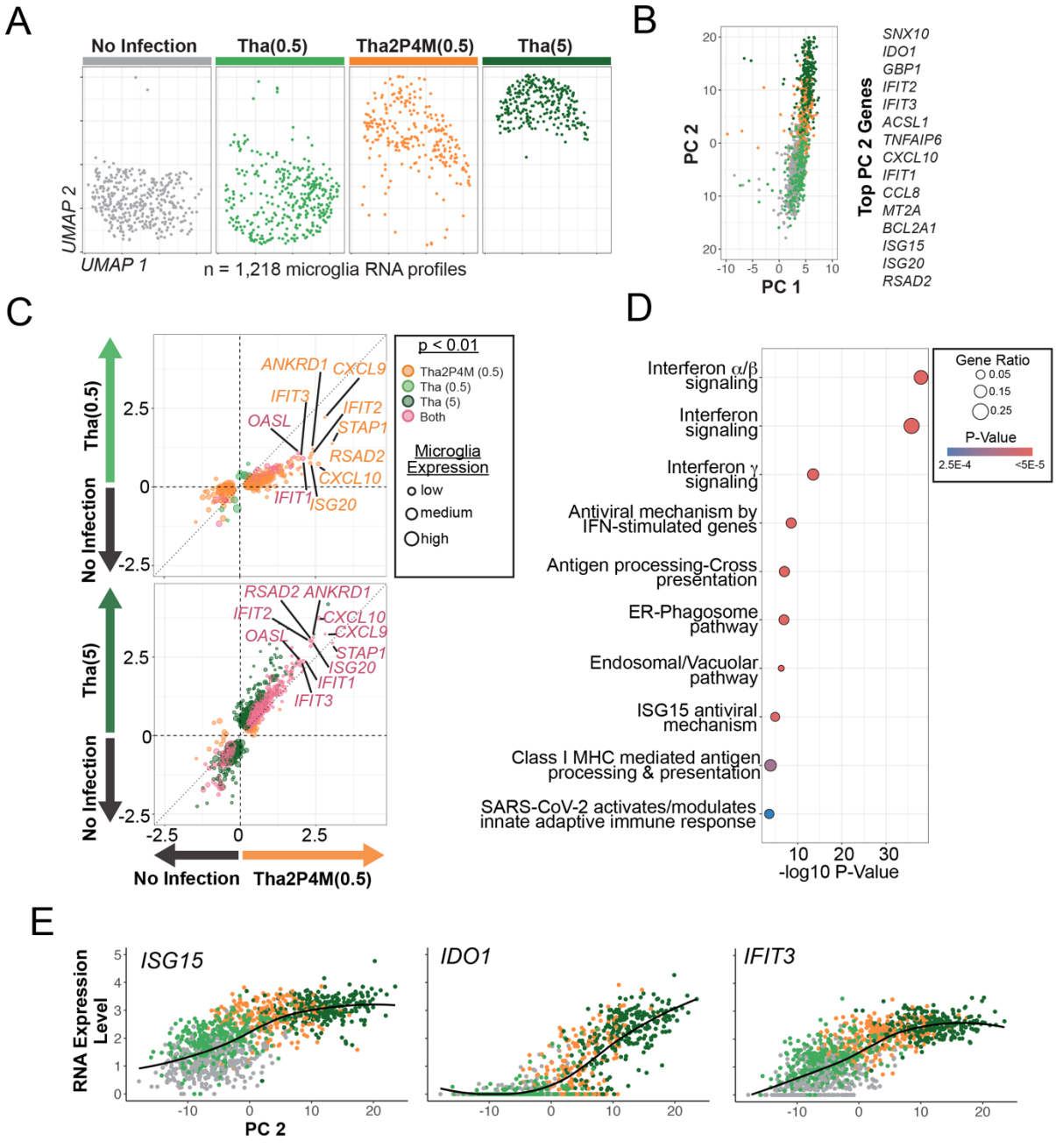

Figure 7. Uninfected microglia respond to Tha RABV infection through graded interferon stimulated gene transcription potentiated by higher viral titer and disinhibited innate immune signalling of other infected cell types.

(A) UMAP embedding plot of microglia scRNA profiles stratified by experimental condition (**Methods**)(n=1,218 cells).

(B) Principal component analysis of variably expressed microglia genes. *Left*, cell component loadings of PC 1 (contamination of neuronal RNAs; **Figure S7B**) versus PC 2 (interferon stimulated gene expression; **Figure S7B**). *Right*, n=15 genes with the highest gene loadings for PC 2.

(C). Scatter plots comparing log2 fold expression level changes of differentially expressed genes ($p < 0.01$) across No Infection microglia and microglia from various experimental conditions (*top*, Tha(0.5) versus Tha2P4M(0.5); *bottom*, Tha(5) versus Tha2P4M(0.5)). Color reflects significant genes shared across comparisons (pink) versus those unique to experimental conditions.

(D) REACTOME pathway analysis plot based on n=202 shared genes found differentially expressed in comparisons of both Tha2P4M(0.5) and Tha(5) to No Infection microglia.

(E) Normalized gene expression plots for three representative interferon stimulated genes plotted against principal component 2 scores and color-coded by experimental condition.

Supplemental Figures

A

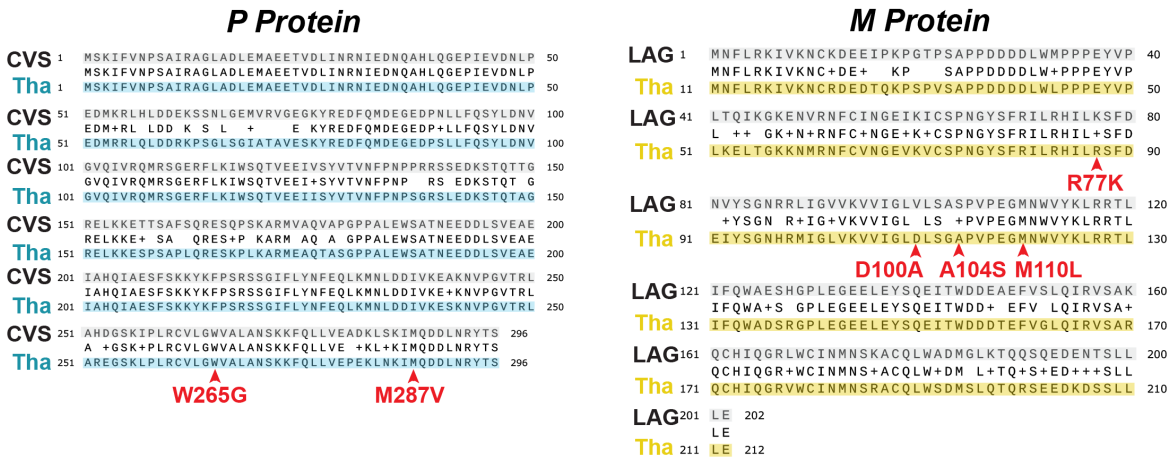

Supplemental Figure 1. RABV P and M protein alignments and locations of 2P4M mutations.

(A) Amino acid-based protein alignments comparing Tha RABV P and M proteins versus those protein sequences from the solved structures shown in **Figure 1E** (CVS P[62] (PDB Accession 1vyi) and Lagos Bat M[63] (PDB Accession 2w2s). The sites of the "2P" and "4M" mutations are shown in red.

1156

A

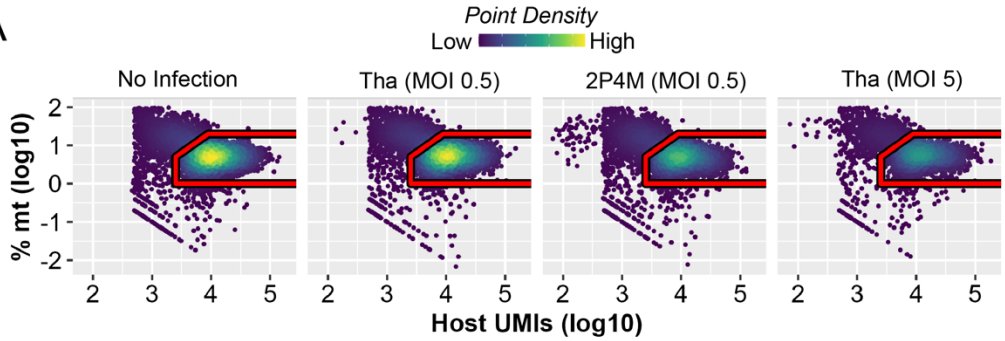

B

Condition	*No Infection*	*Tha (MOI 0.5)*	*Tha2P4M (MOI 0.5)*	*Tha (MOI 5)*	*Total*
Experimental Replicates	3	3	2	2	10
Passing Cells	7,324	7,026	5,064	4,043	23,457

C

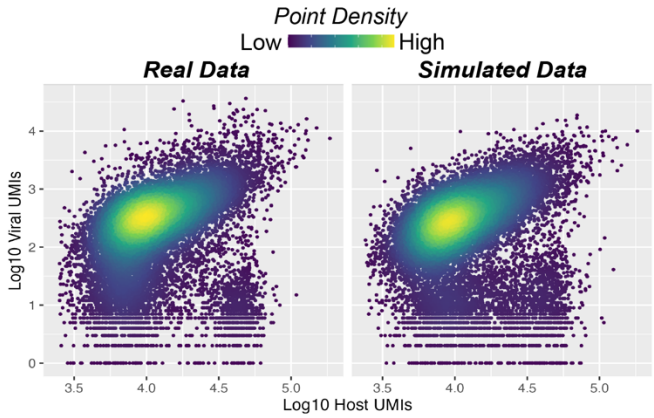

D

1157

1158 **Supplemental Figure 2. Identifying molecular cell types and Tha RABV infection states**
1159 **using single-cell RNA-seq.**

1160 **(A)** Quality-control metrics for inclusion of scRNA profiles. Density scatter plots compare the
1161 size of RNA libraries (based on total human UMI counts) versus the fraction of RNA derived
1162 from the mitochondrial genome. The red polygons define high-quality RNA libraries included
1163 for downstream analysis. Colored heat map indicates point density.

1164 **(B)** Table summarizing the number of RNA profiles and biological replicates for each
1165 experimental condition.

(C) Heat map depiction of expression levels of select marker genes for transcriptional clusters associated with major human brain cell types. Colored heat map indicates expression level. Cells are downsampled by cell type for visualization.

(**D**) Density plot-based comparison of the real versus simulated data of viral versus total UMI counts, demonstrating the accuracy of the model used for Expectation-Maximization identification of RABV infected versus uninfected cells (**Methods**).

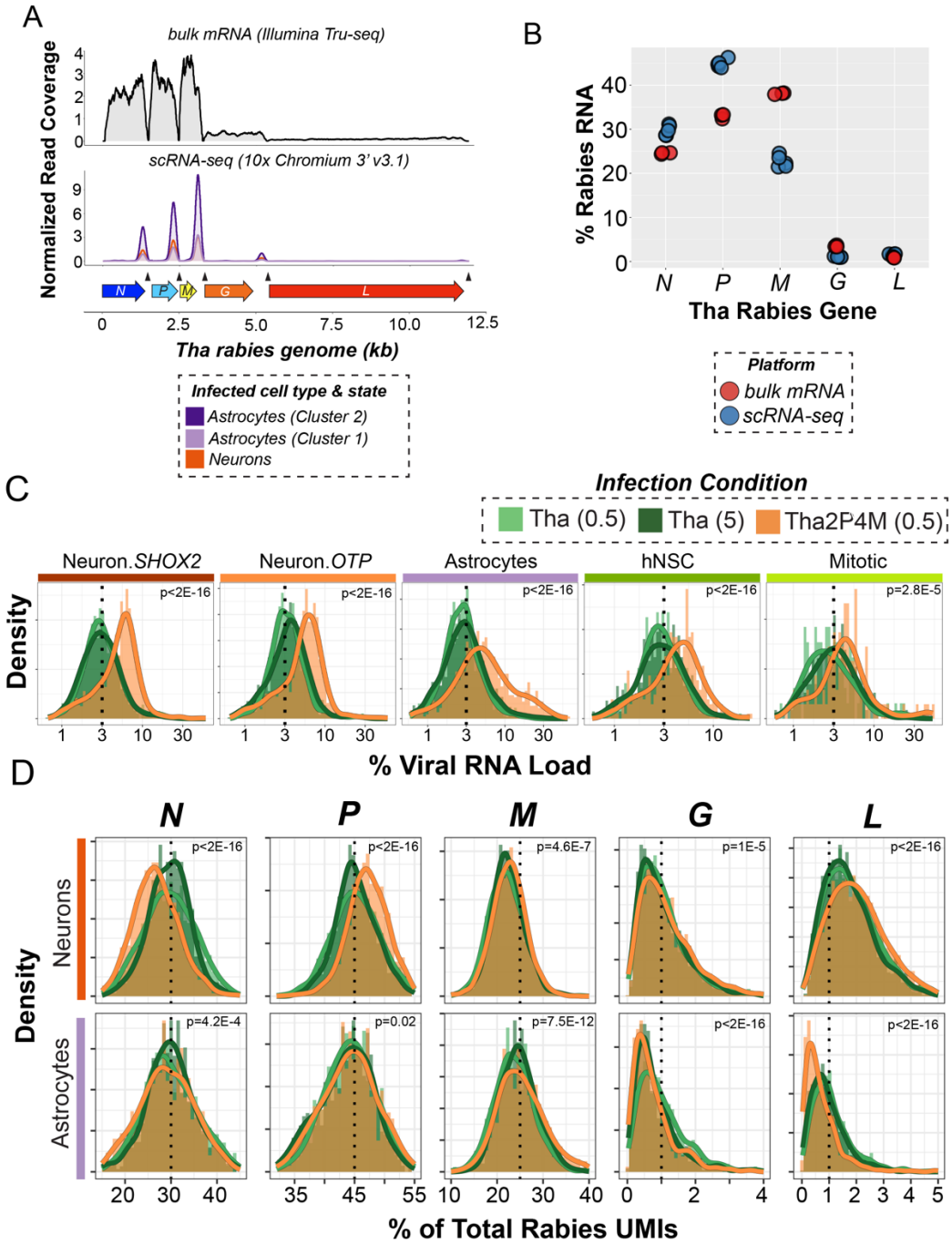

Supplemental Figure 3. RNA expression analysis of Tha RABV genes

(A) Comparison of normalized sequencing read coverage across the Tha RABV genome for bulk RNA sequencing (*top*) following poly A capture and enrichment[30] versus subsets of n=10 scRNA-profiles associated with Neurons and Cluster 1 and Cluster 2 Astrocytes (*bottom*)(Fig. 5; **Methods**). A schematic of the Tha RABV genome is shown at bottom and the locations of polyadenylation signals are shown with arrows.

(B) Comparison of relative expression levels for each Tha RABV gene based on bulk RNA sequencing (red; three biological replicates) versus the scRNA-seq analysis used in this study

(blue; five total biological replicates, n=3 Tha(0.5) and n=2 Tha(5) aggregated across all cell types).

(C) Density plots of viral RNA load stratified by brain cell types and color-coded by experimental condition. P values reporting differences in distributions by experimental condition are reported in each panel (Kruskal-wallis tests).
(D) Density plots of relative RNA levels for each of the five Tha RABV genes color-coded by experimental condition and stratified by both gene and neuron or astrocyte identity. P values reporting differences in gene expression distributions by experimental condition are reported for neurons and astrocytes in each panel (Kruskal-wallis tests).

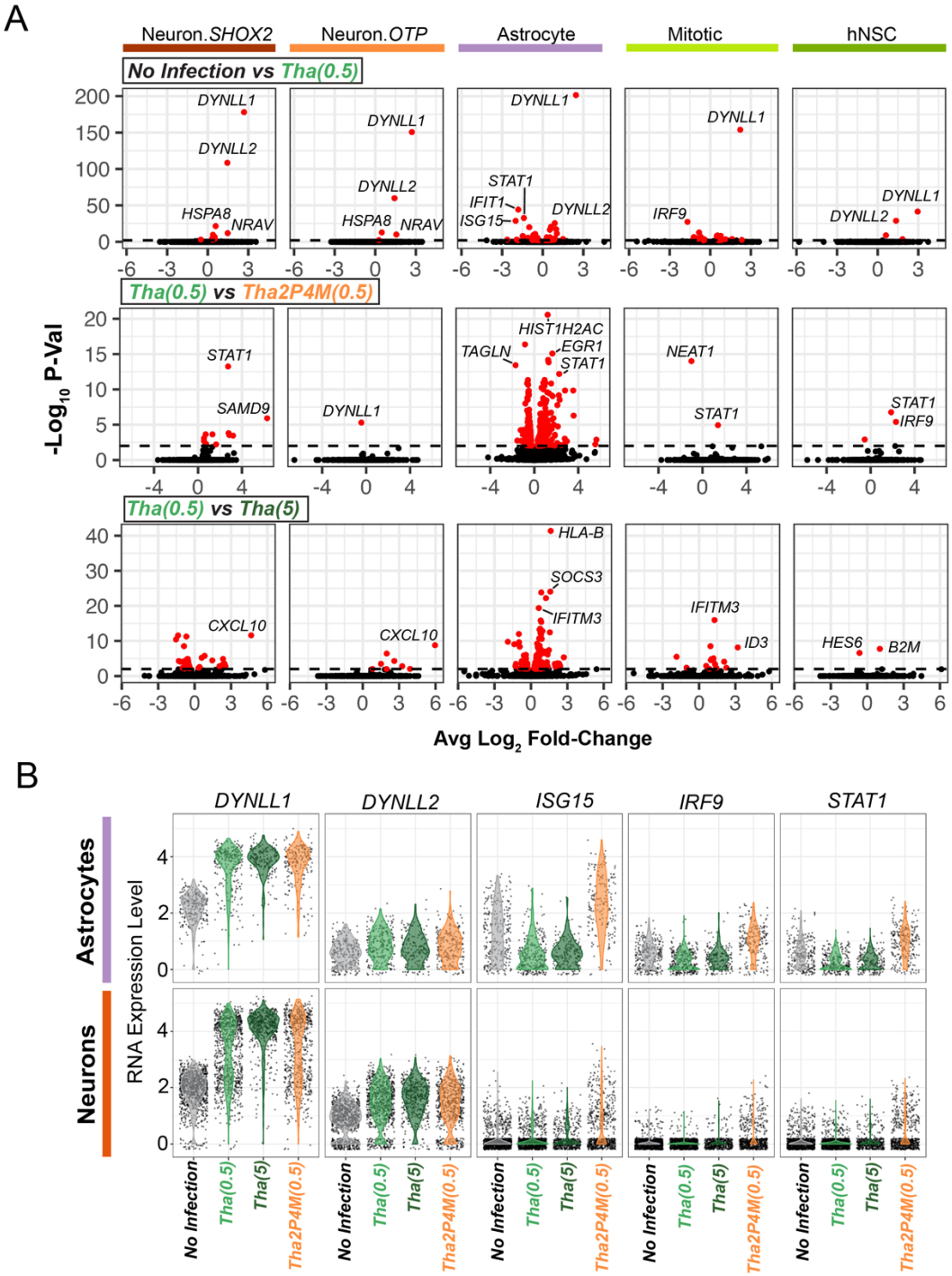

Supplemental Figure 4. Host cell gene expression responses to Tha versus Tha2P4M RABV infection.

(A) Volcano plots of genome-wide expression differences stratified by cell type and experimental condition (*top row*, No Infection versus Tha(0.5); *middle row*, Tha(0.5) versus Tha2P-4M(0.5); *bottom row*, Tha(0.5) versus Tha(5)). Select genes with significant differences (red, $p < 0.01$) are labelled for clarity.

(B) Combined violin dot plots stratified by neurons or astrocytes illustrating RNA expression levels for key genes stratified by experimental condition. (RNA levels are shown as after log-normalization and centering following the default Seurat workflow; **Methods**).

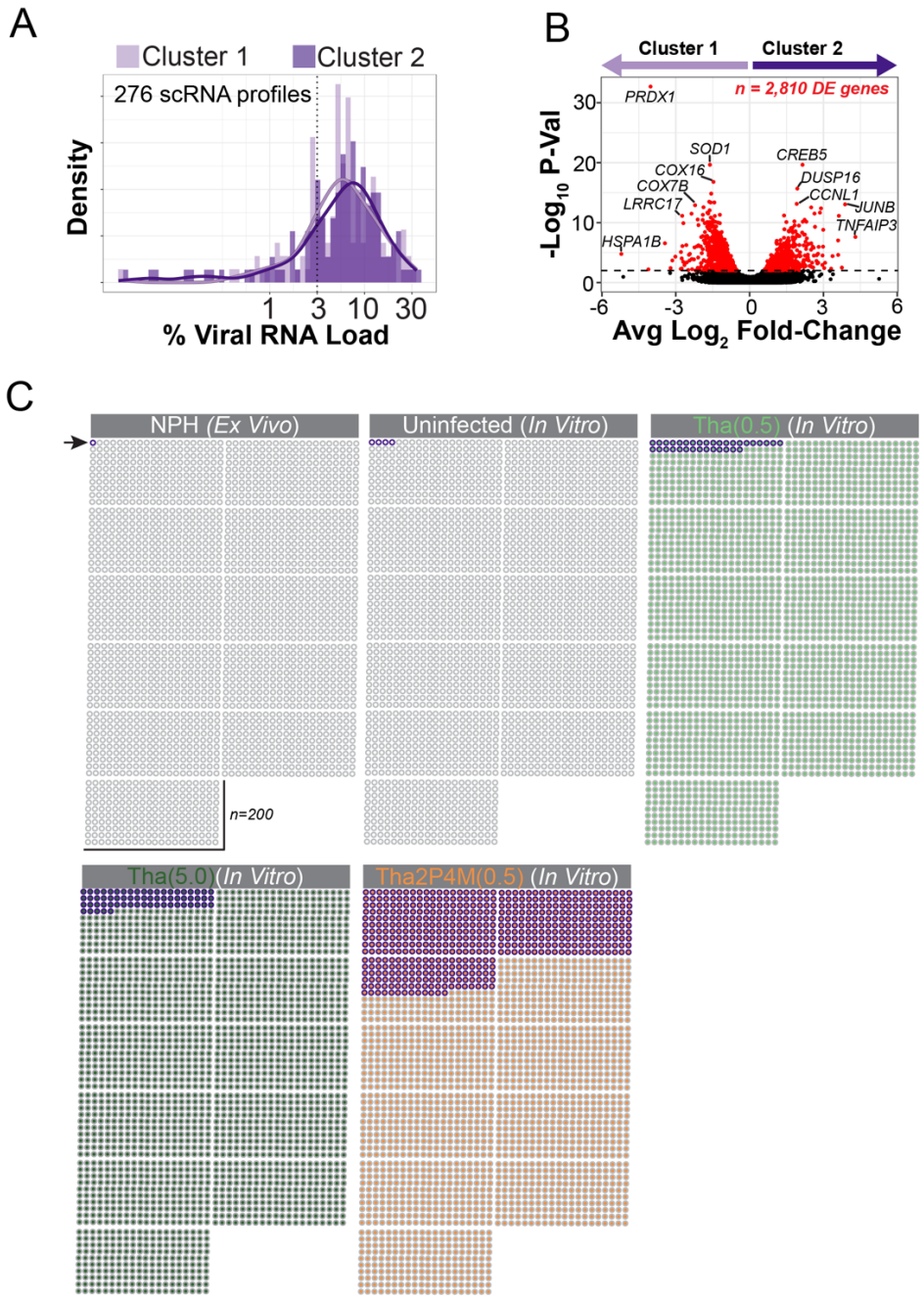

Supplemental Figure 5. Large-scale gene expression changes driving pro-viral Cluster 2 astrocytes occur independently of viral RNA load.

(A) Combined histogram and density plot of viral RNA load distributions for Cluster 1 and 2 after downsampling each cluster to n=276 scRNA profiles with equivalent viral load distributions (**Methods**).

(B) Volcano plots of gene expression differences across viral RNA load downsampled Cluster 1 and 2 with select genes labelled (red, $p < 0.01$).

(C) Schematic approximating the abundance of astrocytes in the Cluster 2 (or Cluster 2-like) pro-viral state across experimental conditions estimated from the NPH and Tha datasets. Circles representing 2,200 astrocytes are shown. The experimental state is indicated by the dot fill, while the Cluster 2/Cluster 2-like state is indicated by a purple outline (beginning at top left, as indicated by the arrow).

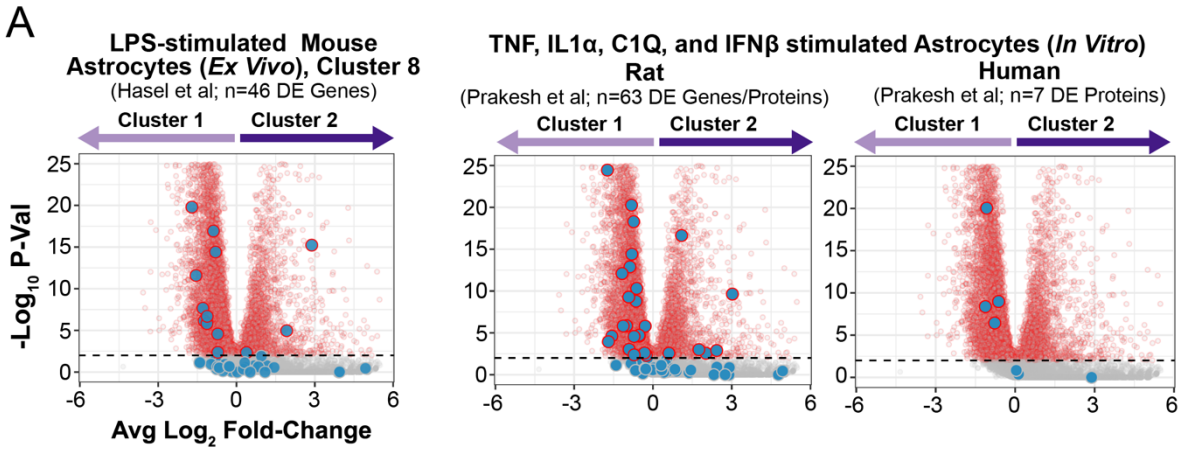

Supplemental Figure 6. Gene expression signatures observed in pro-viral Cluster 2 astrocytes are not observed in previous descriptions of "reactive" rodent or human astrocytes.

(A) Plots of differentially expressed RNAs or proteins from previous studies plotted on volcano plot of depicting expression differences across Cluster 1 and Cluster 2 astrocytes. The size and color of dots represents the intersection of differentially expressed RNAs or proteins from previous studies with those RNAs differentially expressed across Cluster 1 or Cluster 2. Large blue dots correspond to previously described as differentially expressed gene/protein sets (p , 0.01); those with red outlines are also significant in the Cluster 1 versus Cluster 2 comparison ($p < 0.01$). Smaller dots correspond to those genes observed as differentially expressed across Cluster 1 and Cluster 2 (red, $p < 0.01$; grey, $p >= 0.01$) but are not observed as differentially expressed in previous studies. *Left*, 46 genes differentially expressed following scRNA-seq analysis of mouse cortical astrocytes *ex vivo* with an IFN activated gene signature following Lipopolysaccharides (LPS) stimulation. Primary rat (*middle*) or iPSC-derived human (*right*) astrocytes cultured *in vitro* and stimulated with TNF, IL1α, C1Q and IFNβ to induce an interferon-responsive state. The 63 rat genes show concordant changes from bulk RNA-seq and proteomic analysis; the 7 human genes showed alterations based on proteomic analysis only (bulk RNA-seq was not performed).

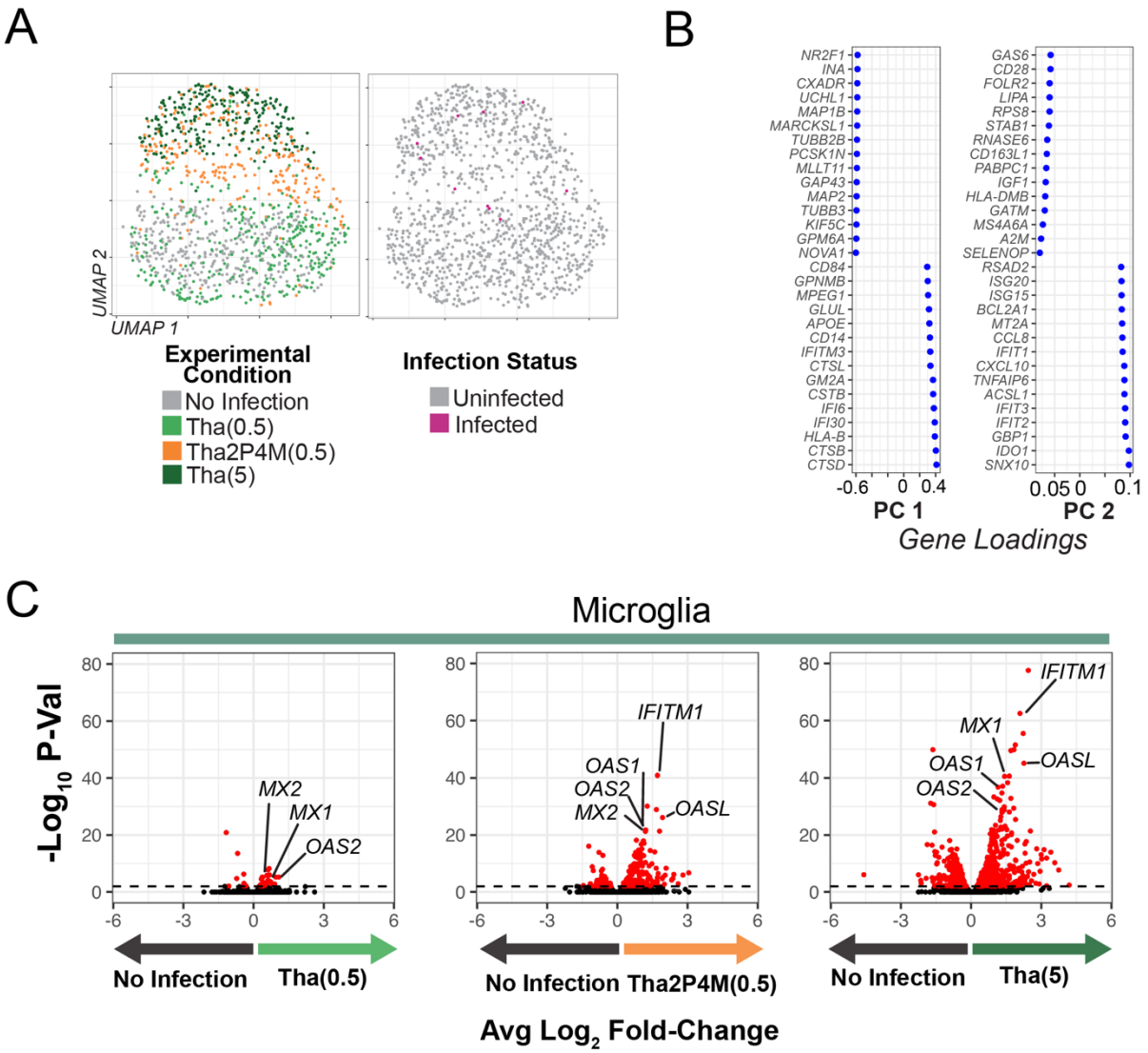

Supplemental Figure 7. Microglia transcriptional response to Tha RABV infection of other cell types.

(A) UMAP embedding plot of microglia scRNA profiles color-coded by experimental condition (*left*) and infection status (*right*).

(B) Gene principal component loading scores for the top and bottom n=15 genes for PC 1 and PC 2. PC 1 genes suggest contamination of neuronal transcripts, while PC 2 genes represent genes transcriptionally regulated by interferon signalling.

(C) Volcano plots of gene expression differences with select genes labelled (red, $p < 0.01$). The corresponding fold-change values for these analyses are shown in **Figure 7C**.

1356 ## Supplemental Table

1357 **Supplemental Table S1** contains all differential gene expression testing results reported in
1358 the manuscript.

1359

1360 ## Supplemental information

1361 ## STAR Methods

1362 ### KEY RESOURCES TABLE

REAGENT or RESOURCE	SOURCE	IDENTIFIER
Antibodies		
Mouse anti-TUBB3	Sigma	Cat# T858
Rabbit anti-GLAST	Invitrogen	Cat# PA5-111080
Rabbit anti-IBA1	Proteintech	Cat# 10904-1-AP
Goat Anti-mouse DYLIGHT 549	KPL	Cat# 072-04-18-06
Goat anti-rabbit Alexa Fluor 549	Invitrogen	Cat# A11035
Virus strains		
Tha RABV (8743THA)	Delmas et al.[65]	GenBank No. EU293121
Tha-eGFP RABV (based on 8743THA)	Besson et al. [66]	Ref-SKU: 014V-03195
Tha2P4M RABV (based on 8743THA)	Sonthonnax et al.[14]	N/A
Chemicals, peptides, and recombinant proteins		
Ascorbid acid	Sigma-Aldrich	Cat# A4403
BMP-4	R&D Systems	Cat# 314-BP-050
B-27 serum free supplement	Thermo Fisher	Cat#17504044
CHIR99021	TOCRIS	Cat# 4423
CSF-1	R&D Systems	Cat# 216-MC-01M
Dead Cell Removal Kit	Miltenyi Biotec	Cat# 130-090-101
DKK-1	R&D Systems	Cat# 5439-DK-500
EGF	Thermo Fisher	Cat# PHG0311
fetal bovine serum (heat inactivated)	Eurobio	Cat# S182H-500
FGF	Thermo Fisher	Cat# PHG0026
FGF-2	R&D Systems	Cat# 223-FB-500
Geltrex	Invitrogen	Cat# A1413201
Glutamax	Thermo Fisher	Cat# 35050038
Hoescht 33342	Thermo Fisher	Cat# H1399
IL-3	R&D Systems	Cat# 203-IL-050
IL-6	R&D Systems	Cat# 206-IL-050
IL-34	R&D Systems	Cat# 5265-IL-010
Knock-out D-MEM/F-12	Thermo Fisher	Cat# A1370801
Laminin	Sigma-Aldrich	Cat# L2020
Neurobasal medium	Thermo Fisher	Cat# 10888022
Papain	Sigma-Aldrich	Cat# P4762
PBS	Thermo Scientific	Cat# 10010023
Penicillin/Streptomycin	Thermo Fisher	Cat# 15140148
Poly-ornithine	Sigma-Aldrich	Cat# P4957
ROCK inhibitor Y-27632	Stemcell Technologies	Cat# ACS-3030
SCF	R&D Systems	Cat# 255-SC-01M
StemPro Accutase	Thermo Scientific	Cat# A1110501
StemPro Neural Supplement	Thermo Fisher	Cat# A1050801

Triton-X	Millipore	Cat# 648463
VEGF	R&D Systems	Cat# 293-VE-500
Critical commercial assays		
Chromium Next GEM Single Cell 3' Kit v3.1	10x Genomics	Cat#: 1000121
Single Index Kit T Set A, 96 rxn	10x Genomics	Cat#: PN-2000240
NovaSeq 6000 S4 Reagent Kit v1.5 (300 cycles)	Illumina	Cat#: 20028312
Deposited data		
scRNA-seq data (raw)	This paper	GEO: GSE284262
scRNA-seq data (processed)	This paper	https://drive.google.com/drive/folders/1Qnv4TorlnZ5z_Z6yzBMwJAIleGyXP9x9?usp=drive_link
Tha bulk mRNA seq data (raw)	Kim et al.	GEO: GSE178583
NPH snRNA sequencing data (processed)	Gazestani et al.	https://zenodo.org/records/8319719
Mouse astrocyte scRNA-seq (processed)	Hasel et al.	PMID: 34413515 (Supp. Table 5)
Rat astrocyte RNA-seq/proteomics (processed)	Prakash et al.	PMID: 8031883 (Supp. Table 5)
Human astrocyte proteomics (processed)	Prakash et al.	PMID: 8031883 (Supp. Table 5)
Experimental models: Cell lines		
Human neural stem cells (EnStem-A™)	Millipore	Cat#: SCC003
XCL-1 iPSC	XCell Science	Cat#: IP-001-1V
Software and algorithms		
R programming language (v4.3.0)	N/A	https://cran.r-project.org/
Python programming language (v3.8.19)	N/A	https://www.python.org/
STAR (v2.7.9a)	Dobin et al.[67]	https://github.com/alexdobin/STAR
RSEM (v1.3.1)	Li et al.[68]	https://github.com/deweylab/RSEM
CellRanger (v5.0.1)	10x Genomics	https://github.com/10XGenomics/cellranger
Seurat (v4.4.0)	Hao et al.[69]	https://cran.r-project.org/
tidyverse (v2.0.0)	Wickham et al.[70]	https://cran.r-project.org/
dplyr (v1.1.4)	Wickham et al.[71]	https://cran.r-project.org/
ggplot2 (v3.5.1)	Wickham[72]	https://cran.r-project.org/
Matrix (v1.6-4)	N/A	https://cran.r-project.org/
viridis (v0.6.5)	N/A	https://cran.r-project.org/
Libra (v1.0.0)	N/A	https://github.com/neurorestore/Libra
clusterProfiler (v4.8.3)	Xu et al.[73]	https://bioconductor.org/
enrichplot (v1.2.3)	Yu[74]	https://bioconductor.org/
ReactomePA (v1.44.0)	Yu et al.[75]	https://bioconductor.org/
ggrepel (v0.9.5)	Slowikowski[76]	https://cran.r-project.org/
ggtree (v3.8.2)	Yu et al.[77]	https://cran.r-project.org/
smplot2 (v0.2.4)	Min et al.[78]	https://bioconductor.org/
qs (v0.26.3)	N/A	https://cran.r-project.org/
data.table (v1.15.4)	Barrett et al.[79]	https://cran.r-project.org/
cowplot(v.1.1.3)	N/A	https://cran.r-project.org/
CellPhoneDB (v5.0)	Troulé et al.[64]	
circlize (v0.4.16)	Gu et al.[80]	https://cran.r-project.org/
PupillometryR (v0.0.5)	Forbes et al.[81]	https://cran.r-project.org/
Snapgene (v7.2.1)	Dotmatics	www.snapgene.com

RESOURCE AVAILABILITY

Lead contact

Further information and viral reagent requests will be fulfilled by lead contacts Dr. Arpiar Saunders and Dr. Herve Bourhy.

Materials availability

Tha RABV reagents are available from Dr. Herve Bourhy with a completed MTA and appropriate lab safety and import restrictions.

Data and code availability

The scRNA-seq datasets generate for this study are available from Gene Expression Omnibus Accession GSE284262. All analysis scripts are available from the Saunders Lab Github () and processed data are also available (https://drive.google.com/drive/folders/1Qnv4TorlnZ5z_Z6yzBMwJAIleGyXP9x9?usp=drive_link).

EXPERIMENTAL MODEL AND SUBJECT DETAILS

Ethics Statement

All Tha RABV *in vitro* infections were performed under BSL3 containment in accordance with the biosafety protocols developed and approved by the Pasteur Institute.

Human brain cell type co-culture

Human neural stem cell culture and differentiation

Human neuronal stem cells (hNSC, EnStem-A™ SCC003, Millipore) were amplified on plates previously cultured with geltrex (A1413201, Invitrogen) in complete neural stem cell (CNSC) medium containing Knock-out D-MEM/F-12 (A1370801, Thermo Fisher), 2 mM Glutamax (35050038, Thermo Fisher), 2% StemPro Neural Supplement (A1050801, ThermoFisher), 20 ng/ml human FGF (PHG0026, Thermo Fisher), and 20 ng/mL human EGF (PHG0311, Thermo Fisher) at 37°C and 5% CO_2. For differentiation, hNSC cells were seeded at a density of $1.5x10^5$ cells/cm^2 on plates previously coated with poly-ornithine (P4957, Sigma-Aldrich) and laminin (L2020, Sigma-Aldrich). One day after seeding, the medium was changed to differentiation medium containing neurobasal medium (10888022, Thermo Fisher), 2 mM Glutamax (35050038, Thermo Fisher), 2% B-27 serum free supplement (17504044, Thermo Fisher), 200 μM Ascorbid acid (A4403, Sigma-Aldrich) and 1x Penicillin/Streptomycin (15140148, Thermo Fisher). Human NSC were differentiated for one week before hiMacs were added to the culture. Half of the medium was changed every third day.

Differentiation of hiPSCs to hiMacs

Human induced macrophage-like cells (hiMacs) were generated from iPSCs according to a published method described by Takata *et al*[82]. In short, 5 ng/mL BMP-4 (314-BP-050, R&D Systems), 50 ng/mL VEGF (293-VE-500, R&D Systems), 2 μM CHIR99021 (4423, TOCRIS) induced mesoderm specification of human iPSC colonies (XCL-1) and hemangioblast-like cell formation (36). Replacement of CHIR99021 by 20 ng/mL FGF-2 (223-FB-500, R&D Systems), followed by maintenance in 15 ng/mL VEGF and 5 ng/mL FGF-2 induced differentiation into the hematopoietic lineage according to a modified protocol from Grigoriadis *et al.* (37). Wnt signalling was inhibited and hematopoietic stem cells were matured by incubation with 50 ng/ml SCF (255-SC-01M), 10 ng/mL FGF-2, 20 ng/mL IL-3 (203-IL-050, R&D Systems), 10 ng/mL

1411 IL-6 (206-IL-050, R&D Systems), 10 ng/mL VEGF and 30 ng/mL DKK-1 (5439-DK-500) for 6
1412 days and with 50 ng/mL SCF, 10 ng/mL FGF-2, 20 ng/mL IL-3 and 10 ng/mL IL-6 for 4 days.
1413 To promote terminal differentiation of hiMacs, cells were cultured with 50 ng/mL CSF-1 (216-
1414 MC-01M, R&D Systems) for 14 days (38–40).

1415 ***Differentiation of hiMacs to hiMicros***

1416 After hiMacs generation, hiMacs were co-cultured with 70 – 80 % confluent one week old (day
1417 0 = induction of neural induction) hiNeurons and hiAstrocytes for three consecutive weeks. In
1418 detail, 7 days after the induction of neural differentiation, $1x10^4$ cells/cm^2 hiMacs were added
1419 to the $1.5x10^5$ cells/cm^2 hiNeurons and hiAstrocytes. Half of the culture medium was changed
1420 every third day supplemented with 50 ng/mL recombinant human CSF-1 (216-MC-010, R&D
1421 Systems) and 50 ng/mL human IL-34 (5265-IL-010, R&D Systems). Cells were co-cultured for
1422 three consecutive weeks before infection experiments were started.

1423 **Tha RABVs**

1424 Thailand virus, referred to as 8764THA (Genbank No. EU293111) is a field strain of RABV
1425 isolated from the brain of a Thai patient who died of RABV after being bitten by a rabid dog
1426 (EVAg collection, Ref-SKU: 014V-02106) (29). This virus was further adapted to cell culture
1427 on BSR cells (a BHK-21 clone, kindly provided by Monique Lafon, Institute Pasteur, Paris)
1428 (32), consequently called 8743THA (Genbank No. EU293121) (29) and in this manuscript
1429 referred to as "Tha". The recombinant Tha2P4M RABV harbors the same genetic background
1430 as Tha apart from bearing two point mutations in the viral P-protein (W265G, M287V) and four
1431 mutations in the viral M-protein (R77K, D100A, A104S, M110L) which were previously
1432 described (15,21,33). To validate viral infection, recombinant viral Tha-eGFP and Th2P4M-
1433 eGFP constructs were used which were generated by cloning sequences of eGFP (recovered
1434 from pEGFP-C1 plasmid, Promega) into the genetic sequence of Tha (34) and Th2P4M,
1435 respectively. Viral strains were sequenced before used for infection experiments. Viral titers
1436 were determined by virus titration on BSR cells via staining of the viral nucleoprotein (5100,
1437 Sigma-Aldrich).
1438

1439 **METHOD DETAILS**

1440 **Visualizing 2P4M mutations on P and M protein structures**

1441 ChimeraX (v1.8)[83] was used to highlight the P protein (W265G, M287V) substitutions on the
1442 structure of the P protein from RABV CVS-11 strain (Protein Data Bank Accession: 1vyi) and
1443 four mutations in the M protein (R77K, D100A, A104S, M110L) on the M protein from Lagos
1444 bat virus (Protein Data Bank Accession: 2W2S). Amino acid alignments (using the CLUSTALW
1445 algorithm implemented in SnapGene (v7.2.1)) confirmed the conserved site positions of each
1446 mutation across *lyssavirus* species and strains (**Figure S1B**).
1447

1448 **Tha RABV infection conditions**

1449 After four weeks of differentiation *in vitro*, co-cultured human brain cells were subject to Tha
1450 RABV infection through bath-application of Tha RABV (diluted in 500 ul of differentiation
1451 media) versus mock infections (500 ul of differentiation media alone) for two hours at 37°C and
1452 5% CO_2. To visualize infected cells and confirm identities of infected cell types, Tha RABV
1453 expressing GFP (Tha-eGFP, MOI 0.5) was used following post-hoc immunofluorescence
1454 analysis. To generate co-cultures upstream of single-cell RNA sequencing, infections were
1455 performed with Tha (MOI 0.5 or 5.0), Tha2P-4M (MOI 0.5) or "No Infection" (mock infection)
1456 were performed.

1457 **Immunofluorescence-based identification of Tha RABV infected cell types**
1458 Forty-eight hours post-infection, co-cultures were fixed using 4% PFA for 15 minutes at room
1459 temperature. After fixation, cells were then washed with PBS (10010023, Thermo Scientific)
1460 and permeabilized using 0.5% triton X-100 (648463, Millipore) for 10 minutes. Immunolabeling
1461 was performed with primary and secondary antibodies (Key resources table) using the
1462 following staining conditions: Cells were stained with the primary antibody diluted in PBS
1463 (10010023, Thermo Scientific) supplemented with 5% heat-inactivated fetal bovine serum
1464 (S182H-500, Eurobio) overnight at 4°C according to the manufacturer's instructions.
1465 Subsequently, cells were washed using PBS (10010023, Thermo Scientific), followed by
1466 staining with the secondary antibody for 30 minutes at 37°C according to the manufacturer's
1467 instructions. Immunolabeled cultures were washed using PBS (10010023, Thermo Scientific)
1468 and imaged using the Opera Phenix™ High Content Screening System (Perkin Elmer) using
1469 standard conditions.

1470 **Single-cell RNA sequencing data generation and processing**
1471 Forty-eight hours after infection, cells were dissociated using StemPro Accutase (A1110501,
1472 Thermo Scientific) supplemented with 50 U/mL papain (P4762, Sigma Aldrich). In detail, cells
1473 were incubated in 400 μl dissociation solution for 10 minutes at 37°C. After 10 minutes, cells
1474 were resuspended in neurobasal medium (10888022, Thermo Fisher) supplemented with 2%
1475 heat-inactivated fetal bovine serum (S182H-500, Eurobio) and 10 μM ROCK inhibitor Y-27632
1476 (ACS-3030, Stemcell Technologies). Cells were centrifuged at 1000 *rpm* for 5 minutes at 4°C.
1477 Viability was increased by removing dead cells via the Dead Cell Removal Kit (130-090-101,
1478 Miltenyi Biotec). In short, cells were resuspended in 100 μl of dead cell removal beads. After
1479 15 minutes of incubation, 400 μl of binding buffer was added to each sample. Samples were
1480 added to the freshly washed LS columns (130-042-401, Miltenyi Biotec). Columns were
1481 washed with 4.5 mL binding buffer (Miltenyi Biotec) and the flow-through was collected. After
1482 the collection of viable cells, cells were centrifuged at 1000 *rpm* for 5 minutes at 4°C.
1483 Meanwhile, viable cells were counted and diluted to a final concentration of 1000 cells/μl.
1484 10,000 cells were loaded per condition using the Chromium Next GEM Single Cell 3' Reagent
1485 Kit v3.1 (PN-1000128, 10x Genomics). The 10x libraries were sequenced at a depth of 40,000
1486 reads per cell using the Illumina NovaSeq Instrument (Novogene). CellRanger (10x Genomics;
1487 v5.0.1) was used to align reads against a composite human (GRCh38) and Tha RABV
1488 genome. Digital Gene Expression (DGE) matrices were generated using reads mapped to
1489 gene exons.

1490 **scRNA-seq workflow for analysis of Tha RABV and human gene expression**
1491 Single-cell RNA-seq data was analyzed in two distinct ways to study human and viral gene
1492 expression in an independent manner and in a synergistic manner in which viral and human
1493 RNAs were associated with the same RNA profiles using experiment-specific cell barcodes.
1494 First, to study human gene expression patterns without the influence of Tha RABV RNAs, Tha
1495 RABV genes were removed to create human-specific DGEs. Human-specific DGEs across all
1496 experimental conditions were filtered based on quality control metrics (described below) and
1497 then processed using a standard workflow in Seurat (v4.4.0)[69] to clustering RNA profiles,
1498 revealing cell type identities. Specifically, scRNA libraries were filtered to include those libraries
1499 with >2,500 UMIs and % of mitochondrial RNAs meeting custom thresholds based on library
1500 size (**Figure S2A**; range: 1-19.9 %). UMI counts in each library were then log-normalized
1501 (*NormalizeData(normalization.method = "LogNormalize", scale.factor = 10000)*) and
1502 expression values for each gene were centered (*ScaleData()*). Clustering was then performed
1503 after variable gene selection (*FindVariableFeatures()* and *RunPCA()*), using n=15 principal

components as input for shared nearest-neighbor graph construction (*FindNeighbors(dims=1:15)*). Clustering was then performed with the smart local moving algorithm (*FindClusters(resolution=0.12)*) and a UMAP embedding was generated (*RunUMAP(dims=1:15, min.dist=0.4))* for visualization. Cell type identities for each cluster were assigned by evaluating the expression patterns of well-established cell-type-specific marker genes for neurons, astrocytes, microglia, neural stem cells and mitotic cell (**Figure S2B**). Second, an "infection summary" file was generated to study Tha RABV gene expression at single-cell resolution. The summary infection file includes UMI counts for each Tha RABV gene as well as total Tha RABV and grand total UMIs (human + Tha). Cell type and infection-status identities (see below) were then assigned to the Tha infection file using experiment-specific cell barcodes for downstream analysis. Importantly, to avoid confounds of low-quality libraries, only those RNA profiles passing the quality-control metrics and included in the final Seurat analysis were included for analyses of Tha gene expression. After global clustering analysis, astrocyte and microglia cellular RNA profiles were independently analyzed in Seurat using a similar workflow. In each case, subclustering revealed minor groups of RNA profiles that exhibited gene expression signatures of other cell types or high-levels of nuclear lncRNAs and thus were removed as candidate "doublets" or low-quality cellular RNA profiles.

Identification of infected and uninfected cells using expectation-maximization

The observed Tha RABV viral RNA UMI counts were modelled as a mixture of two compound log-normal-binomial distributions, one for each of the populations of infected and uninfected cells. These compound distributions were also regressed by the total UMIs for each profile (i.e. library size), allowing the model to account for differences infectivity across cell type populations with varying library sizes. Specifically, letting *LS = library size (total Tha + human UMIs)*, *VL = viral load (% of UMIs from Tha)*, and *VC = viral counts (total Tha UMIs)*, for a given cell with index *i* we draw:

*VL_i ~ logNormal (mu_offset + mu_coef * log (LS_i), sigma_offset + sigma_coef * log(LS_i))*

and then:

VC_i ~ Binom (VL_i, LS_i)

where the parameters *mu_offset*, *mu_coef*, *sigma_offset*, and *sigma_coef* are learned separately for the populations of infected and uninfected cells. The conjugate prior distribution for the binomial distribution is the beta distribution, but we found the beta distribution to fit the expression data poorly, which we hypothesize is due to numerical instability arising from the extreme skew towards low viral load in our data. We chose instead to use a log-normal distribution as the prior distribution for VL, with the additional restriction 0 <= VL <= 1. (In practice, the missing/erroneous probability density from VL > 1 is negligible). Parameter learning was accomplished with a standard expectation-maximization algorithm, first randomly assigning each cell to one of two groups, which we will later categorize as infected or uninfected. For the maximization step, we fit a log-normal-binomial compound distribution (via maximum likelihood estimation) for each population of cells, as well as estimating the priors for each cell belonging to either group. To find maximum likelihood estimates for the log-normal-binomial distributions, we computed and maximized likelihood using the R language optimizer "optim" function, with "method = 'Nelder-Mead'" and starting parameters `mu_off = -4, mu_coef = -0.1, sigma_off = 1.5, sigma_coef = 0`. The probability density for the log-normal-binomial distribution was computed by grid approximation (using 200 points evenly spaced between [-15, 0] and exponentiated). For the expectation step, each cell was assigned to the fitted model from the previous step that maximized its posterior probability. Then new

compound log-normal-binomial distributions were fit to the reassigned groups of cells, and the cells recategorized, repeating this process until convergence (n=20 iterations).

Gene expression plotting

Gene expression levels were plotted using normalized, gene-centered data using functions from Seurat or custom plotting functions using the "ggplot2" (v3.5.1)[72] R package.

Bulk and scRNA-seq analysis of Tha read alignment and gene expression

We re-analyzed bulk mRNA expression data from Tha RABV infection of BSR cells (Gene Expression Omnibus accession GSE178583) in addition to Tha RABV scRNA-seq data from human brain cell type co-cultures to compare Tha RABV gene expression levels and read alignment locations across sequencing modalities (**Figure S3A,B**). Bulk mRNA sequencing data was generated with the TruSeq Stranded mRNA library kit (Illumina). In the previous publication[30], bulk mRNA data were aligned and analyzed with respect to only the human genome (reference GRCh38). Thus STAR (v2.7.9a)[67] was used to realign the bulk mRNA fastq files to both the human and Tha genomes followed by RSEM (v1.3.1)[68] to quantify Tha RABV gene expression levels using transcripts per million reads (TPM) values. Sequencing read coverage against the Tha genome was assessed for the bulk mRNA data and ten randomly selected cell barcodes from the scRNA-seq associated with the neurons, cluster 1 and pro-viral cluster 2 astrocytes. To do this, BAM files associated with these specific read sets were converted to bigwig files then read alignment coordinates were exported to csv files for analysis in R.

Tha RABV gene expression analysis from scRNA-seq data

Viral RNA load scores were calculated for each cell's RNA profile as the percentage of total UMIs (human + Tha) attributed to the five genes in Tha RABV genome (*N, P, M, G* and *L*). Relative expression of each Tha RABV gene was calculated based on the UMIs associated with each gene versus the total Tha RABV UMIs for each cellular RNA profile. To avoid biases driven by insensitive mRNA detection, analysis was limited to cellular RNA profiles with > 0 UMIs for *G* and *L* (the Tha genes with the lowest expression levels; **Figure S3B**). A one-way ANOVA was used to test for differences in Tha gene expression levels, while a two-way ANOVA was used to evaluate if cell type and experimental condition affected relative expression of each Tha gene. Pairwise testing of differences Tha gene expression by cell type and experimental condition was performed using the Kolmogorov–Smirnov test. P values are reported as uncorrected.

Differential expression testing

Human gene differential expression testing across experimental conditions or cell types was implemented in the "Libra" (v1.0.0) R package using the DESeq2 likelihood ratio test method (*Libra::run_de(de_method="DESeq2", de_type="LRT")*). All reported and analyzed p values are corrected for multiple hypothesis testing using the Benjamini-Hochberg method.

Gene Set Enrichment and REACTOME analysis

Gene Set Enrichment Analysis (GSEA) and REACTOME Analysis were performed using the "clusterProfiler" (v4.8.3)[73] and the ReactomePA(v1.44)[75] R packages, respectively. GSEA assessed the "Biological Pathways" ontology using a gene-specific score based on multiplying the -log10(p value) * log2FC for each gene across Tha2P4M(0.5) versus Tha(0.5) astrocytes (*clusterProfiler::gseGO(ont = 'BP',OrgDb = 'org.Hs.eg.db', eps=1e-300)*). The ten Biological

1599 Pathways with strongest enrichment scores visualized using the enrichplot (v1.20.3) R
1600 package (*enrichplot::gseaplot2(= 1:10, ES_geom = "line"*). REACTOME analysis was
1601 performed on differentially expressed gene sets ($p < 0.01$) enriched in either Cluster 1 (n=2,137
1602 genes) or Cluster 2 (n=5,887 genes) Astrocytes ($p < 0.01$)
1603 (ReactomePA::enrichPathway(pvalueCutoff = 0.01). To discern structure within complex
1604 REACTOME results, hierarchical clustering was performed for the most enriched REACTOME
1605 categories Cluster 1 ($p < 0.000001$; n = 32 categories) and Cluster 2 ($p < 0.01$; n = 84
1606 categories) based on similarities of gene driving each categorical enrichment. These results
1607 were visualized using the treeplot() function from the enrichplot (v1.20.3) R package.
1608 REACTOME p values are computed from the hypergeometric distribution using a one-sided
1609 Fisher's exact test and corrected for multiple comparisons using the Benjamini–
1610 Hochberg method.
1611

1612 **Analysis of cell-cell interaction using CellPhoneDB**

1613 "CellPhoneDB"[64] (v5.0; implemented in Python v3.8.19) was used to infer "relevant"
1614 differences in cell-cell interactions between Cluster 1 and pro-viral Cluster 2 astrocytes across
1615 the scRNA-seq dataset. Specifically, "relevant" interactions were identified from the list of
1616 differentially expressed genes comparing Cluster 1 and pro-viral Cluster 2 ($p < 0.01$; LFC > 1;
1617 n= 2,186 enriched in Cluster 1; n= 877 enriched in Cluster 2), a subset of which encode ligands
1618 (n=427) or receptors (n=341). "Relevant" interactions were those that were selectively enriched
1619 in either astrocyte cluster following the CellPhoneDB gene shuffling approach across all cell-
1620 type clusters (neurons, microglia, hNSC and mitotic) from full scRNA-seq dataset ($p < 0.05$).
1621 The "relevant_interactions" CellPhoneDB output file was used for downstream analysis,
1622 visualization and plotting in R including, the R package "circlize" (v0.4.16)[80].
1623

1624 **Identification of pro-viral Cluster 2-like Astrocytes in the NPH snRNA-seq dataset**

1625 To test for evidence of pro-viral Cluster 2-like astrocytes in the human brain without confounds
1626 of post-mortem interval, we took advantage of a published snRNA-seq dataset profiled from
1627 flash-frozen cortical tissue acquired during surgical treatment of Normal Pressure
1628 Hydrocephalus[46]. We used RNA count data and associated patient-specific metadata from the
1629 subset of snRNA-seq profiles belonging to astrocytes (n= 82,634 profiles;
1630 https://zenodo.org/records/8319719). The RNA count data were cell-normalized and gene-
1631 centered using the standard Seurat workflow (equivalent to the processing performed on the
1632 Tha scRNA-seq dataset). To identify potential Cluster 2-like astrocytes from these NPH data,
1633 we generated an aggregate expression score based on the n=196 genes observed in the NPH
1634 data and enriched in Cluster 2 ($p < 0.01$ and 2 > log2 fold-change). To critically evaluate the
1635 biological significance of these aggregate expression scores, we generated 1,000 expression-
1636 matched sets of 196 genes. Expression-matching was performed by rank-ordering the NPH
1637 genes by expression level; dividing these expression-ranked genes into ten bins from low to
1638 high expression; and randomly sampling (without replacement) each bin by the number of
1639 instances of each of the 196 Cluster 2 enriched genes. To facilitate comparison of the real and
1640 permuted aggregate gene score distributions, each of 82,634 scores were z-scored by gene
1641 list and z-score distributions were then analyzed (**Figure 5H**). A z-score threshold of 4.5
1642 standard deviations was used to identify n=38 Cluster 2-like NPH astrocytes contributed by
1643 n=21 of 52 total patients (n=1 to 4 Cluster 2-like NPH astrocytes in each of those 21 patients;
1644 z-score range: 4.5 – 12.5). The cut-off of 4.5 standard deviations corresponds to a p-value of
1645 < 4.7E-7 based on the permuted data. To validate these 38 astrocyte RNA profiles resembled
1646 those of Cluster 2, we tested whether gene counts associated with the 196 "discovery" gene

set and an independent "validation" gene set of RNAs enriched in Cluster 2 ($p < 0.01$ and 1-2 log2 fold-change; n=521 genes) were enriched in the 38 Cluster 2-like astrocytes versus all other NPH astrocyte RNA profiles (n=82,596). The discovery and validation gene counts were 2.8 and 1.2 enriched respectively in the 38 Cluster 2-like NPH astrocytes and highly significant (chi-square test of expected versus observed UMIs; $p < 1E-16$).

Comparing "reactive" astrocyte gene signatures from other datasets to pro-viral Cluster 2 astrocytes

To assess the similarity of previously reported rodent and human reactive astrocyte gene expression signatures to those observed in pro-viral Cluster 2 astrocytes, we re-analyzed data from *ex vivo* mouse astrocytes stimulated with lipopolysaccharides (Hasel et al; scRNA-seq data)[48] or cultured rat and human astrocytes stimulated with TNF, IL1α, C1Q, and IFNβ, a cocktail that induces an interferon-responsive reactive state (Prakash et al; RNA and proteomic profiling)[47]. Specifically, for Hasel et al, gene enrichment data from the ten scRNA-seq-defined astrocyte clusters were downloaded (Supplementary Table 5). Analysis focused on those genes enriched in cluster 8 (n=70 genes), an astrocyte sub-population described by Hasel et al as "interferon reactive"[48]. For Prakash et al, RNA and protein enrichments associated with rat and human interferon-responsive state were downloaded (Supplementary Tables 3 and 5). Analysis focused on the n=67 rat genes with concordant, statistically-significant enrichments in both RNA and protein; for human astrocytes, analysis focused on the n=8 genes enriched via proteomic analysis (RNA expression data was not acquired). The genes from these three lists were visualized on volcano plots describing Cluster 1 versus pro-viral Cluster 2 differentially expressed genes. In all three cases, RNAs from the published gene set showed no obvious enrichments for those genes differentially expressed in Cluster 1 or pro-viral Cluster 2 and thus no statistical test was performed.

Analysis of single-cell RNA sequencing data

Statistical testing and plot generation was performed in R (v4.3.0; R packages are provided in the Key Resources table). All p-values are reported as adjusted for multiple-hypothesis testing unless otherwise stated. Test-specific information is included the relevant STAR Methods sections.

References

1. Hampson, K. *et al.* Estimating the Global Burden of Endemic Canine Rabies. *PLoS Neglected Trop. Dis.* **9**, e0003709 (2015).

2. Schnell, M. J., McGettigan, J. P., Wirblich, C. & Papaneri, A. The cell biology of rabies virus: using stealth to reach the brain. *Nat Rev Micro* 1–11 (2009) doi:10.1038/nrmicro2260.

3. Jackson, A. C., Randle, E., Lawrance, G. & Rossiter, J. P. Neuronal apoptosis does not play an important role in human rabies encephalitis. *J. NeuroVirology* **14**, 368–375 (2008).

4. Suja, M. S., Mahadevan, A., Madhusudana, S. N. & Shankar, S. K. Role of Apoptosis in Rabies Viral Encephalitis: A Comparative Study in Mice, Canine, and Human Brain with a Review of Literature. *Pathol. Res. Int.* **2011**, 374286 (2011).

5. Griffin, D. E. Recovery from viral encephalomyelitis: immune-mediated noncytolytic virus clearance from neurons. *Immunol. Res.* **47**, 123–133 (2010).

1692 6. Yordy, B., Iijima, N., Huttner, A., Leib, D. & Iwasaki, A. A Neuron-Specific Role for
1693 Autophagy in Antiviral Defense against Herpes Simplex Virus. *Cell Host Microbe* **12**, 334–
1694 345 (2012).

1695 7. Potratz, M. *et al.* Astrocyte Infection during Rabies Encephalitis Depends on the Virus
1696 Strain and Infection Route as Demonstrated by Novel Quantitative 3D Analysis of Cell
1697 Tropism. *Cells* **9**, 412–20 (2020).

1698 8. Potratz, M. *et al.* Neuroglia infection by rabies virus after anterograde virus spread in
1699 peripheral neurons. *Acta Neuropathol. Commun.* **8**, 199 (2020).

1700 9. Feige, L. *et al.* Susceptibilities of CNS Cells towards Rabies Virus Infection Is Linked to
1701 Cellular Innate Immune Responses. *Viruses* **15**, 88 (2022).

1702 10. Pfefferkorn, C. *et al.* Abortively Infected Astrocytes Appear To Represent the Main
1703 Source of Interferon Beta in the Virus-Infected Brain. *J Virol* **90**, 2031–2038 (2016).

1704 11. Sofroniew, M. V. Astrocyte Reactivity: Subtypes, States, and Functions in CNS Innate
1705 Immunity. *Trends Immunol.* **41**, 758–770 (2020).

1706 12. Sugamata, M. *et al.* Paralysis of street rabies virus-infected mice is dependent on T
1707 lymphocytes. *J. Virol.* **66**, 1252–1260 (1992).

1708 13. Zhao, P. *et al.* Global gene expression changes in BV2 microglial cell line during rabies
1709 virus infection. *Infect., Genet. Evol.* **20**, 257–269 (2013).

1710 14. Sonthonnax, F. *et al.* Lyssavirus matrix protein cooperates with phosphoprotein to
1711 modulate the Jak-Stat pathway. *Sci. Rep.* 1–13 (2019) doi:10.1038/s41598-019-48507-4.

1712 15. Bertoune, M. A. R. *et al.* The phenotype of the RABV glycoprotein determines cellular
1713 and global virus load in the brain and is decisive for the pace of the disease. *Virology* **511**,
1714 82–94 (2017).

1715 16. Khalifa, Y. B. *et al.* The matrix protein of rabies virus binds to RelAp43 to modulate NF-
1716 κB-dependent gene expression related to innate immunity. *Sci. Rep.* **6**, 39420 (2016).

1717 17. Besson, B. *et al.* Regulation of NF-κB by the p105-ABIN2-TPL2 complex and RelAp43
1718 during rabies virus infection. *PLoS Pathog.* **13**, e1006697 (2017).

1719 18. Vidy, A., Chelbi-Alix, M. & Blondel, D. Rabies Virus P Protein Interacts with STAT1 and
1720 Inhibits Interferon Signal Transduction Pathways. *J Virol* **79**, 14411–14420 (2005).

1721 19. Brzózka, K., Finke, S. & Conzelmann, K.-K. Inhibition of Interferon Signaling by Rabies
1722 Virus Phosphoprotein P: Activation-Dependent Binding of STAT1 and STAT2. *J. Virol.* **80**,
1723 2675–2683 (2006).

1724 20. Lieu, K. G. *et al.* The Rabies Virus Interferon Antagonist P Protein Interacts with
1725 Activated STAT3 and Inhibits Gp130 Receptor Signaling. *J. Virol.* **87**, 8261–8265 (2013).

1726 21. Wang, Z. W. *et al.* Attenuated Rabies Virus Activates, while Pathogenic Rabies Virus
1727 Evades, the Host Innate Immune Responses in the Central Nervous System. *J Virol* **79**,
1728 12554–12565 (2005).

1729 22. Ménager, P. *et al.* Toll-Like Receptor 3 (TLR3) Plays a Major Role in the Formation of
1730 Rabies Virus Negri Bodies. *PLoS Pathog* **5**, e1000315-15 (2009).

1731 23. Lahaye, X., Vidy, A., Fouquet, B. & Blondel, D. Hsp70 Protein Positively Regulates
1732 Rabies Virus Infection. *J Virol* **86**, 4743–4751 (2012).

1733 24. Daugherty, M. D. & Malik, H. S. Rules of Engagement: Molecular Insights from Host-
1734 Virus Arms Races. *Annu. Rev. Genet.* **46**, 677–700 (2012).

1735 25. Vidy, A., Bougrini, J. E., Chelbi-Alix, M. K. & Blondel, D. The Nucleocytoplasmic Rabies
1736 Virus P Protein Counteracts Interferon Signaling by Inhibiting both Nuclear Accumulation and
1737 DNA Binding of STAT1. *J. Virol.* **81**, 4255–4263 (2007).

1738 26. Hossain, Md. A. *et al.* Structural Elucidation of Viral Antagonism of Innate Immunity at the
1739 STAT1 Interface. *Cell Rep.* **29**, 1934-1945.e8 (2019).

1740 27. Harrison, A. R. *et al.* Lyssavirus P-protein selectively targets STAT3-STAT1 heterodimers
1741 to modulate cytokine signalling. *PLoS Pathog.* **16**, e1008767 (2020).

1742 28. Scrima, N. *et al.* Rabies virus P protein binds to TBK1 and interferes with the formation of
1743 innate immunity-related liquid condensates. *Cell Rep.* **42**, 111949 (2023).

1744 29. Wiltzer, L. *et al.* Interaction of Rabies Virus P-Protein With STAT Proteins is Critical to
1745 Lethal Rabies Disease. *J. Infect. Dis.* **209**, 1744–1753 (2014).

1746 30. Kim, S. *et al.* Early Transcriptional Changes in Rabies Virus-Infected Neurons and Their
1747 Impact on Neuronal Functions. *Front Microbiol* **12**, 730892 (2021).

1748 31. Abraham, G. & Banerjee, A. K. Sequential transcription of the genes of vesicular
1749 stomatitis virus. *Proc. Natl. Acad. Sci.* **73**, 1504–1508 (1976).

1750 32. Ball, L. A. & White, C. N. Order of transcription of genes of vesicular stomatitis virus.
1751 *Proc. Natl. Acad. Sci.* **73**, 442–446 (1976).

1752 33. Ball, L. A. Transcriptional mapping of vesicular stomatitis virus in vivo. *J. Virol.* **21**, 411–
1753 414 (1977).

1754 34. Zhang, D. *et al.* Genome-Wide Transcriptional Profiling Reveals Two Distinct Outcomes
1755 in Central Nervous System Infections of Rabies Virus. *Front. Microbiol.* **7**, 118–16 (2016).

1756 35. Huang, K. W. & Sabatini, B. L. Single-Cell Analysis of Neuroinflammatory Responses
1757 Following Intracranial Injection of G-Deleted Rabies Viruses. *Front Cell Neurosci* **14**, 65
1758 (2020).

1759 36. Kotliar, D. *et al.* Single-Cell Profiling of Ebola Virus Disease In Vivo Reveals Viral and
1760 Host Dynamics. *Cell* **183**, 1383-1401.e19 (2020).

1761 37. Merino-Gracia, J., García-Mayoral, M. F. & Rodríguez-Crespo, I. The association of viral
1762 proteins with host cell dynein components during virus infection. *FEBS Journal* **278**, 2997–
1763 3011 (2011).

1764 38. Raux, H., Flamand, A., virology, D. B. J. of & 2000. Interaction of the rabies virus P
1765 protein with the LC8 dynein light chain. *Am Soc Microbiol*.

1766 39. Tan, G. S., Preuss, M. A. R., Williams, J. C. & Schnell, M. J. The dynein light chain 8
1767 binding motif of rabies virus phosphoprotein promotes efficient viral transcription. *Proc Natl*
1768 *Acad Sci* **104**, 7229–7234 (2007).

1769 40. Poisson, N. *et al.* Molecular basis for the interaction between rabies virus phosphoprotein
1770 P and the dynein light chain LC8: dissociation of dynein-binding properties and
1771 transcriptional functionality of P. *J. Gen. Virol.* **82**, 2691–2696 (2001).

1772 41. Bauer, A., Nolden, T., Nemitz, S., Perlson, E. & Finke, S. A Dynein Light Chain 1 Binding
1773 Motif in Rabies Virus Polymerase L Protein Plays a Role in Microtubule Reorganization and
1774 Viral Primary Transcription. *J. Virol.* **89**, 9591–9600 (2015).

1775 42. Jurado, S. *et al.* ATM Substrate Chk2-interacting Zn2+ Finger (ASCIZ) Is a Bi-functional
1776 Transcriptional Activator and Feedback Sensor in the Regulation of Dynein Light Chain
1777 (DYNLL1) Expression*. *J Biol Chem* **287**, 3156–3164 (2012).

1778 43. Bauer, A., Nolden, T., Nemitz, S., Perlson, E. & Finke, S. A Dynein Light Chain 1 Binding
1779 Motif in Rabies Virus Polymerase L Protein Plays a Role in Microtubule Reorganization and
1780 Viral Primary Transcription. *J Virol* **89**, 9591–9600 (2015).

1781 44. Lahaye, X., Vidy, A., Fouquet, B. & Blondel, D. Hsp70 Protein Positively Regulates
1782 Rabies Virus Infection. *J. Virol.* **86**, 4743–4751 (2012).

1783 45. Ouyang, J. *et al.* NRAV, a Long Noncoding RNA, Modulates Antiviral Responses through
1784 Suppression of Interferon-Stimulated Gene Transcription. *Cell Host Microbe* **16**, 616–626
1785 (2014).

1786 46. Gazestani, V. *et al.* Early Alzheimer's disease pathology in human cortex involves
1787 transient cell states. *Cell* **186**, 4438-4453.e23 (2023).

1788 47. Prakash, P. *et al.* Proteomic profiling of interferon-responsive reactive astrocytes in
1789 rodent and human. *Glia* **72**, 625–642 (2024).

1790 48. Hasel, P., Rose, I. V. L., Sadick, J. S., Kim, R. D. & Liddelow, S. A. Neuroinflammatory
1791 astrocyte subtypes in the mouse brain. *Nat Neuro* 1–36 (2021) doi:10.1038/s41593-021-
1792 00905-6.

1793 49. Linder, A. *et al.* Defective Interfering Genomes and the Full-Length Viral Genome Trigger
1794 RIG-I After Infection With Vesicular Stomatitis Virus in a Replication Dependent Manner.
1795 *Front. Immunol.* **12**, 595390 (2021).

1796 50. Aouadi, W. *et al.* Comparative analysis of rabies pathogenic and vaccine strains
1797 detection by RIG-I-like receptors. *Microbes Infect.* **26**, 105321 (2024).

1798 51. Cavalieri, R. L., Havell, E. A., Vilcek, J. & Pestka, S. Induction and decay of human
1799 fibroblast interferon mRNA. *Proc. Natl. Acad. Sci.* **74**, 4415–4419 (1977).

1800 52. Tan, G. S., Preuss, M. A. R., Williams, J. C. & Schnell, M. J. The dynein light chain 8
1801 binding motif of rabies virus phosphoprotein promotes efficient viral transcription. *Proc. Natl.*
1802 *Acad. Sci.* **104**, 7229–7234 (2007).

1803 53. Rehwinkel, J. & Gack, M. U. RIG-I-like receptors: their regulation and roles in RNA
1804 sensing. *Nat. Rev. Immunol.* **20**, 537–551 (2020).

1805 54. Chelbi-Alix, M. K., Vidy, A., Bougrini, J. E. & Blondel, D. Rabies Viral Mechanisms to
1806 Escape the IFN System: The Viral Protein P Interferes with IRF-3, Stat1, and PML Nuclear
1807 Bodies. *Journal of Interferon & Cytokine Research* **26**, 271–280 (2006).

1808 55. Patani, R., Hardingham, G. E. & Liddelow, S. A. Functional roles of reactive astrocytes in
1809 neuroinflammation and neurodegeneration. *Nat. Rev. Neurol.* **19**, 395–409 (2023).

1810 56. Escartin, C. *et al.* Reactive astrocyte nomenclature, definitions, and future directions. *Nat.*
1811 *Neurosci.* **24**, 312–325 (2021).

1812 57. Tian, B. *et al.* Lab-Attenuated Rabies Virus Causes Abortive Infection and Induces
1813 Cytokine Expression in Astrocytes by Activating Mitochondrial Antiviral-Signaling Protein
1814 Signaling Pathway. *Front. Immunol.* **8**, 2011 (2018).

1815 58. Krause, T. B. & Cepko, C. L. Abortive and productive infection of CNS cell types following
1816 in vivo delivery of VSV. *Proc. Natl. Acad. Sci.* **121**, e2406421121 (2024).

1817 59. Ray, N. B., Power, C., Lynch, W. P., Ewalt, L. C. & Lodmell, D. L. Rabies viruses infect
1818 primary cultures of murine, feline, and human microglia and astrocytes. *Arch. Virol.* **142**,
1819 1011–1019 (1997).

1820 60. Liu, S. Q., Xie, Y., Gao, X., Wang, Q. & Zhu, W. Y. Inflammatory response and MAPK
1821 and NF-κB pathway activation induced by natural street rabies virus infection in the brain
1822 tissues of dogs and humans. *Virol. J.* **17**, 157 (2020).

1823 61. Zhang, X. *et al.* Derivation of Human Embryonic Stem Cells from Developing and
1824 Arrested Embryos. *Stem Cells* **24**, 2669–2676 (2006).

1825 62. Mavrakis, M., McCarthy, A. A., Roche, S., Blondel, D. & Ruigrok, R. W. H. Structure and
1826 Function of the C-terminal Domain of the Polymerase Cofactor of Rabies Virus. *J. Mol. Biol.*
1827 **343**, 819–831 (2004).

1828 63. Graham, S. C. *et al.* Rhabdovirus Matrix Protein Structures Reveal a Novel Mode of Self-
1829 Association. *PLoS Pathog* **4**, e1000251-12 (2008).

1830 64. Troulé, K. *et al.* CellPhoneDB v5: inferring cell-cell communication from single-cell
1831 multiomics data. *arXiv* (2023) doi:10.48550/arxiv.2311.04567.

1832 65. Delmas, O. *et al.* Genomic Diversity and Evolution of the Lyssaviruses. *PLoS ONE* **3**,
1833 e2057 (2008).

1834 66. Besson, B. *et al.* Kinome-Wide RNA Interference Screening Identifies Mitogen-Activated
1835 Protein Kinases and Phosphatidylinositol Metabolism as Key Factors for Rabies Virus
1836 Infection. *mSphere* **4**, 10.1128/msphere.00047-19 (2019).

1837 67. Dobin, A. *et al.* STAR: ultrafast universal RNA-seq aligner. *Bioinformatics* **29**, 15–21
1838 (2012).

1839 68. Li, B. & Dewey, C. N. RSEM: accurate transcript quantification from RNA-Seq data with
1840 or without a reference genome. *BMC Bioinform.* **12**, 323 (2011).

1841 69. Hao, Y. *et al.* Integrated analysis of multimodal single-cell data. *Cell* **184**, 3573-3587.e29
1842 (2021).

70. Wickham, H. *et al.* Welcome to the Tidyverse. *J. Open Source Softw.* **4**, 1686 (2019).

71. Wickham, H., Francois, R., Henry, L., Kirill & Vaughan, D. dplyr: A Grammar of Data Manipulation. (2023).

72. Wickham, H. *Ggplot2: Elegant Graphics for Data Analysis*. (Springer-Verlag New York, 2016).

73. Xu, S. *et al.* Using clusterProfiler to characterize multiomics data. *Nat. Protoc.* 1–29 (2024) doi:10.1038/s41596-024-01020-z.

74. Yu, G. enrichplot: Visualization of Functional Enrichment Result. *R package version 1.24.4* (2024).

75. Yu, G. & He, Q.-Y. ReactomePA: an R/Bioconductor package for reactome pathway analysis and visualization. *Mol. Biosyst.* **12**, 477–479 (2015).

76. Slowikowski, K. ggrepel: Automatically Position Non-Overlapping Text Labels with "ggplot2." (2024).

77. Yu, G., Smith, D. K., Zhu, H., Guan, Y. & Lam, T. T. ggtree: an r package for visualization and annotation of phylogenetic trees with their covariates and other associated data. *Methods Ecol. Evol.* **8**, 28–36 (2017).

78. Min, S. H. & Zhou, J. smplot: An R Package for Easy and Elegant Data Visualization. *Front. Genet.* **12**, 802894 (2021).

79. Barrett, T. *et al.* data.table: Extension of `data.frame`. (2024).

80. Gu, Z., Gu, L., Eils, R., Schlesner, M. & Brors, B. circlize implements and enhances circular visualization in R. *Bioinformatics* **30**, 2811–2812 (2014).

81. Forbes, S. PupillometryR: An R package for preparing and analysing pupillometry data. *J. Open Source Softw.* **5**, 2285 (2020).

82. Takata, K. *et al.* Induced-Pluripotent-Stem-Cell-Derived Primitive Macrophages Provide a Platform for Modeling Tissue-Resident Macrophage Differentiation and Function. *Immunity* **47**, 183-198.e6 (2017).

83. Meng, E. C. *et al.* UCSF ChimeraX: Tools for structure building and analysis. *Protein Sci.* **32**, e4792 (2023).